

# Explainable Bayesian deep learning through input-skip Latent Binary Bayesian Neural Networks

**Eirik Høyheim**

**Lars Skaaret-Lund**

**Solve Sæbø**

**Aliaksandr Hubin**

*KBM, Bioinformatics and applied statistics (BIAS),  
Norwegian University of Life Sciences*

EIRIK.HOYHEIM@FFI.NO

LARS.SKAARET-LUND@NMBU.NO

SOLVE.SABO@NMBU.NO

ALIAKSANDR.HUBIN@NMBU.NO

## Abstract

Modeling natural phenomena with artificial neural networks (ANNs) often provides highly accurate predictions. However, ANNs often suffer from over-parameterization, complicating interpretation and raising uncertainty issues. Bayesian neural networks (BNNs) address the latter by representing weights as probability distributions, allowing for predictive uncertainty evaluation. Latent binary Bayesian neural networks (LBBNNs) further handle structural uncertainty and sparsify models by removing redundant weights. This article advances LBBNNs by enabling covariates to skip to any succeeding layer or be excluded, simplifying networks and clarifying input impacts on predictions. Ultimately, a linear model or even a constant can be found to be optimal for a specific problem at hand. Furthermore, the input-skip LBBNN approach reduces network density significantly compared to standard LBBNNs, achieving over 99% reduction for small networks and over 99.9% for larger ones, while still maintaining high predictive accuracy and uncertainty measurement. For example, on MNIST, we reached 97% accuracy and great calibration with just 935 weights, reaching state-of-the-art for compression of neural networks. Furthermore, the proposed method accurately identifies the true covariates and adjusts for system non-linearity. The main contribution is the introduction of active paths, enhancing directly designed global and local explanations within the LBBNN framework, that have theoretical guarantees and do not require post hoc external tools for explanations.

## 1. Introduction

In recent years, artificial intelligence (AI) and machine learning (ML) have entered the colloquial language, largely due to the availability of highly sophisticated neural network models like GPT-4 [OpenAI, 2023]. These models are extensions of standard multilayer perceptrons, utilizing more advanced transformer architectures with billions of weights to map inputs to predictions. A key theoretical result associated with ANNs is the universal approximation theorem [Cybenko, 1989, Hornik et al., 1989], which states that an ANN can approximate any given function when provided with sufficient data and given that the number of neurons in the hidden layer is large enough. Hence, there is no surprise that huge GPT-4 models trained on vast amounts of data collected from the internet perform well on approximating common knowledge. Yet, despite these impressive capabilities in function approximation, ANNs lack interpretability due to their complexity, making it difficult to understand predictive uncertainty or the contribution of individual covariates. Moreover,

the lack of uncertainty handling does not facilitate proper "doubt" handling or "I don't know" responses in ANNs like GPT-4 [Papamarkou et al., 2024].

Bayesian neural networks (BNNs) [Neal, 1992] offer a partial solution by incorporating weight uncertainty. BNNs sample weights from the posterior weight distribution each time an input is propagated through the network. This provides the possibility to construct credibility intervals for model parameters and predictions. However, BNNs are computationally more expensive and retain the architectural complexity of ANNs, thus not allowing them to explain their predictions either locally or globally.

Latent binary Bayesian neural networks (LBBNNs) [Hubin and Storvik, 2019, Bai et al., 2020] address complexity by structure learning for model uncertainties. This is done by introducing trainable indicator variables for each weight. Thus, each combination of on and off weights produces a separate model. The probability of inclusion of each weight is then approximated. Finally, heavy sparsification is possible through a median probability model (MPM), which consists of weights with inclusion probabilities above 0.5. Thus, one can drastically reduce weight density by learning the appropriate neural network structure for a given problem. Also, incorporating model uncertainties in addition to parameter uncertainties was empirically shown to provide better predictive calibration for both images and tabular data in Skaaret-Lund et al. [2024]. Despite these important benefits, LBBNN models can still be unnecessarily complex, with thousands of weights and nonlinear transformations, hindering interpretability.

Specifically, the most significant limitation for LBBNNs is that covariates must pass through all hidden layers and nonlinear activation functions even if the MPM is extremely sparse. This approach might be unnecessary, as the underlying relationship between the input and output might be much simpler, i.e. simply linear. Furthermore, using overly complex models complicates interpretability, as more connections must be considered when examining the global explanation of a model. Additionally, larger models with more applications of matrix multiplications than necessary have negative environmental impacts due to the increased computational requirements for predictions and the additional storage space needed to save the models.

Standard LBBNNs force covariates through all layers, obscuring input-output relationships and inflating model size. To address these issues, we extend the LBBNN methods by introducing input-skip, allowing all covariates to enter directly any given layer. This approach enables the model to learn the most optimal structure for the problem at hand. For instance, if the true underlying relationship between the input and output is linear, the learned model should be a linear function, meaning all other weights are redundant and should be removed. Similarly, if the relationship is nonlinear, the model should utilize the appropriate amount of nonlinear activation functions in the hidden layers and ignore all excessive connections in the initialized model. This is in stark contrast to traditional approaches, where one has to decide on a model *a priori*. It also avoids extensive combinatorial exploration like in neural architecture search [Elsken et al., 2019] or in Bayesian generalized nonlinear models [Hubin et al., 2021]. Further, local and global explanation methods are provided for LBBNN with input-skip. These explanations are built into the design of our model and do not need any external approximations like SHAP [Lundberg and Lee, 2017] or SAGE [Covert et al., 2020], thus avoiding both additional expensive computations and using approximations to explain other approximations that do not propagate

uncertainties to the downstream task properly. The innovative input-skip LBBNN approach reduces network density by over 99% for small networks and over 99.9% for larger ones, maintaining high accuracy and uncertainty measurement. Specifically, on MNIST, ISLaB achieves 97% accuracy with just 935 weights, which is a new efficiency frontier compared to prior sparse models like Lottery Ticket ( $\sim 1,300$  weights, 95%) [Frankle and Carbin, 2019]. To summarize, this article introduces the following innovations and contributions:

- An LBBNN method that allows the covariates to skip to any given layer or be entirely excluded from the model, simplifying the network architecture and clarifying input contributions to predictions.
- A novel method that enhances global and local understanding of trained networks, providing deeper insights into the contributions of individual covariates to the overall predictions.

## 2. Materials and Methods

A neural network model connects the output  $\mathbf{y}_i \in \mathbb{R}^c$  to the input  $\mathbf{x}_i \in \mathbb{R}^v$  via a probability distribution parametrized with a trainable mapping  $\zeta(\mathbf{x}_i)$ , as shown in Figure 1:

$$\mathbf{y}_i \sim f(\cdot; \zeta(\mathbf{x}_i), \phi). \quad (1)$$

Here,  $f$  represents the distribution modeling the relationship between covariates and responses through its trainable parameters  $\zeta(\mathbf{x}_i)$  conditioning on the former and known fixed parameters  $\phi$ , which could be the dispersion parameter for instance. For example, in binary classification ( $c = 1$ ), a Bernoulli distribution might be used with  $\zeta(\mathbf{x}_i)$  being the probability of success and  $\phi$  being 1, while a Gaussian distribution with  $\zeta(\mathbf{x}_i)$  consisting of the mean and the variance being  $\phi$  is suitable for regression tasks. For multivariate classification problems ( $c > 2$ ), a categorical distribution is typically assumed. The parameters  $\zeta(\cdot)$ , necessary for these distributions, are obtained by passing the covariates through a composition of hidden layers.

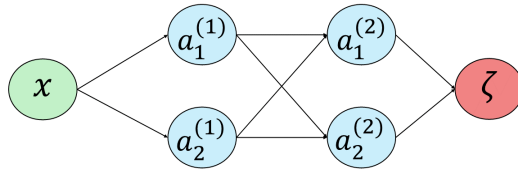


Figure 1: A simple ANN architecture without bias nodes.

Thus, each hidden layer consists of nodes computed using a semi-affine transformation of the signal coming from the preceding layer:

$$a_p^{(j)} = o^{(j)} \left( a_0^{(j-1)} w_{0,p}^{(j)} + \sum_{k=1}^K a_k^{(j-1)} w_{k,p}^{(j)} \right). \quad (2)$$

In Equation (2),  $k = 1, 2, \dots, K$  represents the number of hidden nodes in the preceding layer,  $p = 1, 2, \dots, P$  indicates the number of hidden nodes in the succeeding layer, and  $j = 1, 2, \dots, J$  denotes the layer positions, where 0 is the input layer,  $\mathbf{a}^{(0)} = \mathbf{x}$ , and  $J$  is the output layer,  $\mathbf{a}^{(J)} = \zeta(\mathbf{x}_i)$ . The weight connecting the  $k$ -th node in layer  $j - 1$  to the  $p$ -th node in layer  $j$  is denoted by  $w_{k,p}^{(j)}$ ,  $a_k^{(j-1)}$  is the activation of the  $k$ -th node in layer  $j - 1$ , and  $a_p^{(j)}$  is the activation to be computed for the  $p$ -th node in layer  $j$ . The bias node and its associated weight are represented by  $a_0^{(j-1)}$  and  $w_{0,p}^{(j)}$ , respectively. For all layers,  $a_0^{(j-1)} = 1$ , thus it is omitted in subsequent equations.

## 2.1 Bayesian neural networks

A Bayesian neural network (BNN) is a variation of an ANN where weights are represented as probability distributions instead of scalars, as illustrated in Figure 2.

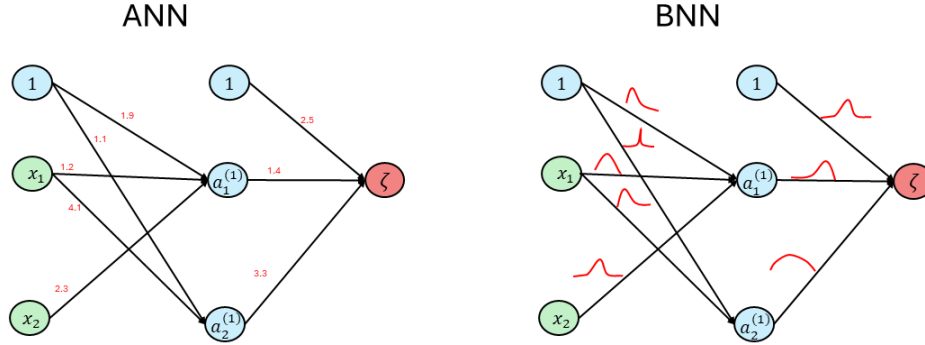


Figure 2: Illustration of simple ANN (on the left) and BNN (on the right) architectures.

In the Bayesian paradigm, all unknown parameters are treated as random variables. Given a prior distribution over the weights,  $p(\mathbf{W})$ , with  $\mathbf{W} = \{w_{k,p}^{(j)}, k = 1, \dots, K, p = 1, \dots, P, j = 1, \dots, J\}$ , a likelihood function  $\mathcal{L}(D|\mathbf{W})$ , and marginal likelihood,  $\mathcal{F}(D)$ , we find the posterior weight distribution  $\pi(\mathbf{W}|D)$  through Bayes' theorem:

$$\pi(\mathbf{W}|D) = \frac{\mathcal{L}(D|\mathbf{W})p(\mathbf{W})}{\mathcal{F}(D)}. \quad (3)$$

Here,  $\mathbf{W}$  represents the weight parameters and  $D$  is the available data. The posterior weight distribution allows making new predictions,  $y_{\text{new}}$ , given unseen data,  $\mathbf{x}_{\text{new}}$  by the posterior predictive distribution:

$$\begin{aligned}
 \pi(y_{\text{new}}|\mathbf{x}_{\text{new}}, D) &= \int_{\mathbf{W}} \pi(y_{\text{new}}, \mathbf{W}|\mathbf{x}_{\text{new}}, D) d\mathbf{W} \\
 &= \int_{\mathbf{W}} \pi(y_{\text{new}}|\mathbf{x}_{\text{new}}, \mathbf{W}, D) \pi(\mathbf{W}|D) d\mathbf{W} \\
 &= \mathbb{E}_{\pi(\mathbf{W}|D)} [\pi(y_{\text{new}}|\mathbf{x}_{\text{new}}, \mathbf{W}, D)].
 \end{aligned} \tag{4}$$

Since exact evaluations of the integral are computationally prohibitive due to the ultra-high dimensionality of  $\mathbf{W}$ , approximations like Monte Carlo (MC) are used:

$$\pi(y_{\text{new}}|\mathbf{x}_{\text{new}}, D) \approx \frac{1}{N} \sum_{i=1}^N \pi(y_{\text{new}}|\mathbf{x}_{\text{new}}, \mathbf{W}_{(i)}, D), \mathbf{W}_{(i)} \sim \pi(\mathbf{W}|D). \tag{5}$$

Equation (5) is the MC approximation of the integral, where random weights,  $\mathbf{W}_{(i)}$ , are drawn  $N$  times from the posterior weight distribution. A credibility interval for the prediction can be obtained as empirical quantiles from these  $N$  samples, allowing to describe the confidence in a prediction.

## 2.2 Latent Binary Bayesian Neural Networks

Neural networks, with their potential to incorporate millions or even billions of weights, present significant challenges in terms of interpretability and computational cost. This complexity is further amplified in BNNs, as weights are represented through probability distributions. To attain more interpretable models, structural reduction in the number of weights within a network is imperative.

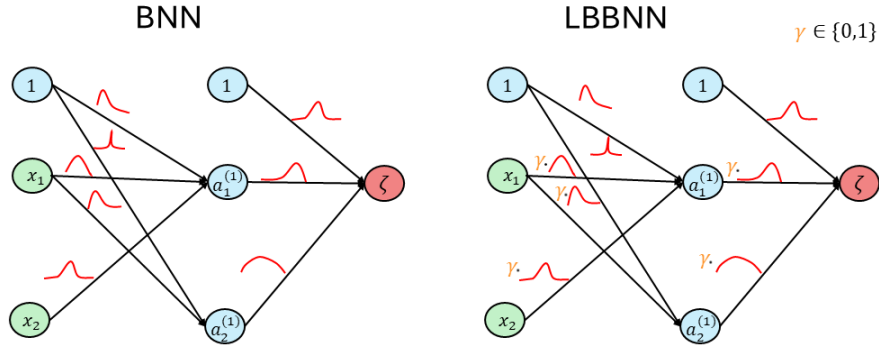


Figure 3: Illustration of the difference between BNNs (left) and LBBNNs (right).

To learn the neural network structures over which weights are required in BNNs, [Hubin and Storvik \[2019\]](#) proposed associating each weight with a trainable latent indicator variable. These indicator variables facilitate sparsification by learning whether a weight should

be included or excluded, and thus identifying an appropriate network structure for a specific problem through the posterior probabilities of weight inclusions allowing for automatic edge pruning. This model, known as latent binary Bayesian neural networks (LBBNNs), incorporates an inclusion parameter,  $\gamma_{k,p}^{(j)} \in \{0, 1\}$ , into the node  $p$  output in a given layer  $j$  of a model as follows:

$$a_p^{(j)} = o^{(j)} \left( w_{0,p}^{(j)} + \sum_{k=1}^K \gamma_{k,p}^{(j)} a_k^{(j-1)} w_{k,p}^{(j)} \right), \quad (6)$$

where  $w_{k,p}^{(j)}$  is an entry of  $\mathbf{W}$  corresponding to the  $k$ -th weight of neuron  $p$  in layer  $j$ . In Equation (6),  $\gamma$  is not included in front of the bias weight, following Skaaret-Lund et al. [2024] and Hubin and Storvik [2024], so the bias distribution remains consistent with the one presented for BNNs. An LBBNN model comprises all weights,  $\mathbf{W}$ , and their associated inclusion parameters  $\gamma_{k,p}^{(j)}$  forming a matrix  $\Gamma$ , that defines the network structure. Thus, we have one extra parameter per weight compared to standard BNNs, but with the potential to prune away a large proportion of the weights by inferring the structure of the MPM. To incorporate both weight and structural uncertainty into an LBBNN model, the spike-and-slab prior is used, assuming independence between weights within and between layers [Hubin and Storvik, 2019, Skaaret-Lund et al., 2024]:

$$p \left( w_{k,p}^{(j)} | \gamma_{k,p}^{(j)} \right) = \gamma_{k,p}^{(j)} \mathcal{N} \left( w_{k,p}^{(j)}; 0, \left( \tau_{k,p}^{(j)} \right)^2 \right) + \left( 1 - \gamma_{k,p}^{(j)} \right) \delta_0 \left( w_{k,p}^{(j)} \right) \quad (7)$$

$$p \left( \gamma_{k,p}^{(j)} \right) = \text{Bernoulli} \left( \gamma_{k,p}^{(j)}; \psi_{k,p}^{(j)} \right), \quad \psi_{k,p}^{(j)} \in [0, 1]. \quad (8)$$

The "spike" part of the prior is denoted by  $\delta_0$ , a probability (mass) at zero, and the "slab" part is represented by a Gaussian distribution in the most common definition, although other continuous distributions can be used, for instance, the wider t-distribution, as in Hubin and Storvik [2024]. The main objective is to find the posterior distribution,  $\pi(\mathbf{W}, \Gamma | D)$ , to make predictions on unseen data. The predictive distribution extends Equation (4) to consider all  $2^{||\Gamma||}$  models forming a model space  $\mathcal{M}$ , where each model is defined by a specific pattern of on and off weights and  $||\Gamma||$  counts the number of elements of the matrix of latent binary indicators. The predictive distribution accounting for model uncertainty is:

$$\pi(y_{\text{new}} | \mathbf{x}_{\text{new}}, D) = \sum_{\Gamma \in \mathcal{M}} \int_{\mathbf{W}} \pi(y_{\text{new}} | \mathbf{x}_{\text{new}}, \mathbf{W}, \Gamma, D) \pi(\mathbf{W}, \Gamma | D) d\mathbf{W}. \quad (9)$$

Even more severely than for standard BNNs, the predictive distribution is unattainable due to the difficulty of obtaining the exact posterior distribution. This makes it more convenient to use an approximate posterior distribution through the variational inference (VI)-based framework.

A common choice for the approximate posterior distribution of  $\pi(\mathbf{W}, \Gamma | D)$  is obtained by factorizing into the product of independent approximations of  $\pi(w_{k,p}^{(j)}, \gamma_{k,p}^{(j)} | D) \approx q_{\eta_{k,p}^{(j)}}(w_{k,p}^{(j)}, \gamma_{k,p}^{(j)}) =$

$q_{\theta_{k,p}^{(j)}}(w_{k,p}^{(j)}|\gamma_{k,p}^{(j)})q_{\alpha_{k,p}^{(j)}}(\gamma_{k,p}^{(j)})$  with  $\eta_{k,p}^{(j)} = (\theta_{k,p}^{(j)}, \alpha_{k,p}^{(j)}) = (\mu_{k,p}^{(j)}, \sigma_{k,p}^{(j)}, \alpha_{k,p}^{(j)})$  through the approximations defined as follows:

$$\begin{aligned} q_{\theta_{k,p}^{(j)}}(w_{k,p}^{(j)}|\gamma_{k,p}^{(j)}) &= \gamma_{k,p}^{(j)} \mathcal{N}(w_{k,p}^{(j)}; \mu_{k,p}^{(j)}, (\sigma_{k,p}^{(j)})^2) + (1 - \gamma_{k,p}^{(j)}) \delta_0(w_{k,p}^{(j)}) \\ q_{\alpha_{k,p}^{(j)}}(\gamma_{k,p}^{(j)}) &= \text{Bernoulli}(\gamma_{k,p}^{(j)}; \alpha_{k,p}^{(j)}), \quad \alpha_{k,p}^{(j)} \in [0, 1]. \end{aligned} \quad (10)$$

This is known as mean-field approximations of LBBNN's posterior [Hubin and Storvik, 2024]. The goal is to find the parameters of the variational posterior,

$$q_{\boldsymbol{\eta}}(\mathbf{W}, \Gamma) = \prod_{k,p,j} q_{\eta_{k,p}^{(j)}}(w_{k,p}^{(j)}, \gamma_{k,p}^{(j)})$$

that makes it as close as possible to the true posterior  $\pi(\mathbf{W}, \Gamma|D)$ , where closeness is typically measured by the KL-divergence. Optimization with respect to the vector of parameters  $\boldsymbol{\eta}$  can be done using numerical optimization algorithms like batch stochastic gradient descent or Adam [Kingma and Ba, 2015]:

$$\begin{aligned} \boldsymbol{\eta}^* &= \arg \min_{\boldsymbol{\eta}} \text{KL}\left(q_{\boldsymbol{\eta}}(\mathbf{W}, \Gamma) \parallel \pi(\mathbf{W}, \Gamma|D)\right) \\ &= \arg \min_{\boldsymbol{\eta}} \int_{\mathbf{W}} \sum_{\Gamma} q_{\boldsymbol{\eta}}(\mathbf{W}, \Gamma) \left( \log \frac{q_{\boldsymbol{\eta}}(\mathbf{W}, \Gamma)}{p(\mathbf{W}, \Gamma)} - \log \mathcal{L}(D|\mathbf{W}, \Gamma) \right) d\mathbf{W} \\ &= \arg \min_{\boldsymbol{\eta}} \text{KL}\left(q_{\boldsymbol{\eta}}(\mathbf{W}, \Gamma) \parallel p(\mathbf{W}, \Gamma)\right) - \mathbb{E}_{q_{\boldsymbol{\eta}}(\mathbf{W}, \Gamma)} \left[ \log \mathcal{L}(D|\mathbf{W}, \Gamma) \right]. \end{aligned} \quad (11)$$

To ensure that  $\alpha$  remains between 0 and 1 during the training process, it is conventional to define  $\alpha = \frac{1}{1+\exp(-\lambda)}$ , where  $\lambda \in \mathbb{R}$ . The reparameterization trick and a gradient-based method are commonly used to find an appropriate  $\boldsymbol{\eta}^*$  efficiently. However, as entries of  $\Gamma$  are binary, the gradient is not differentiable. Solutions include using a relaxation to make entries of  $\Gamma$  continuous [Hubin and Storvik, 2024] or using the local reparameterization trick [Kingma et al., 2015, Skaaret-Lund et al., 2024], with the latter being more computationally efficient due to sampling the (approximate) Gaussian pre-activations directly, in addition to not needing any relaxations.

Mean-field approximations (10) ignore all dependencies in the posterior distributions, which may be not optimal. To resolve this, Skaaret-Lund et al. [2024] additionally suggested to use dependent latent variables for the mean parameters of the approximate posteriors through multiplicative normalizing flows [Louizos and Welling, 2017] within a layer, resulting in the following approximations for a given layer  $j$ :

$$q_{\boldsymbol{\theta}}(\mathbf{W}^{(j)}|\boldsymbol{\Gamma}^{(j)}, \mathbf{z}^{(j)}) = \prod_{p,k} \left( \gamma_{k,p}^{(j)} \mathcal{N}(w_{ij}; z_k^{(j)} \mu_{k,p}^{(j)}, \sigma_{k,p}^{(j)2}) + (1 - \gamma_{k,p}^{(j)}) \delta(w_{k,p}^{(j)}) \right); \quad (12)$$

$$q_{\tilde{\alpha}_{k,p}^{(j)}}(\gamma_{k,p}^{(j)}) = \text{Bernoulli}(\gamma_{k,p}^{(j)}; \alpha_{k,p}^{(j)}), \quad (13)$$

where  $\mathbf{z}^{(j)}$  follows a distribution  $q_\phi(\mathbf{z}^{(j)})$  modeled by normalizing flows [Louizos and Welling, 2017] and thus introduces flexible spatial dependencies between the parameters through multiplicative neuron-specific multiplicative random effects. The details on integrating out  $\mathbf{z}^{(j)}$  in the KL divergence are further provided in Skaaret-Lund et al. [2024].

### 2.3 Input-skip in Latent Binary Bayesian Neural Networks

Input-skip is implemented in LBBNN by concatenating the input covariates to all hidden layers, as illustrated in Figure 4. While concatenation has been previously utilized in convolutional neural networks such as DenseNets [Huang et al., 2017] and U-nets [Ronneberger et al., 2015], as well as in multilayer perceptron models like DenseNet Regression [Jiang et al., 2022] and  $l_1$ -regularized nets [Lundby et al., 2023], this method has never been associated with an LBBNN model. Input-skip for latent binary Bayesian neural networks, hereafter abbreviated ISLaB, is therefore the first of its kind.

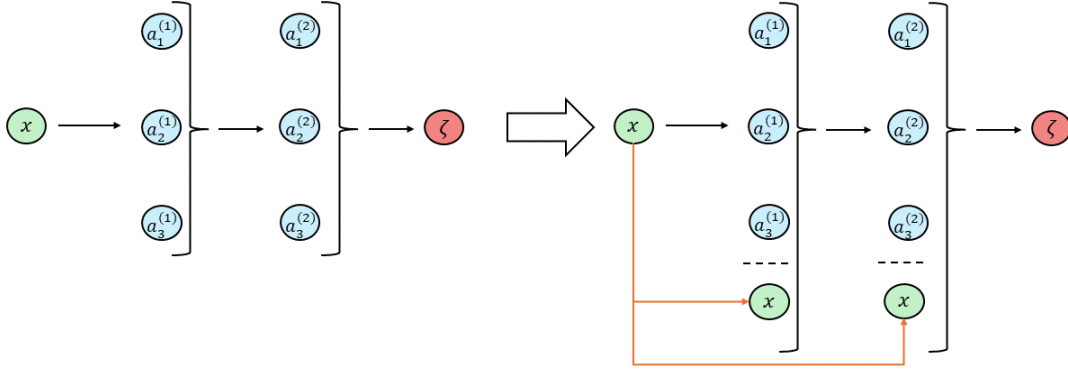


Figure 4: Concatenation is used to allow the input to skip directly to any given hidden layer.

The extension of the LBBNN method to the ISLaB method is as follows:

$$a_p^{(j)} = o^{(j)} \left( w_{0,p}^{(j)} + \sum_{k=1}^{K+v} \gamma_{k,p}^{(j)} a_k^{(j-1)} w_{k,p}^{(j)} \right), \quad (14)$$

where  $v$  is the number of covariates. The main difference between the ISLaB method and the previously implemented LBBNN is that  $a^{(j-1)}$  will be extended to always include the covariates, resulting in:

$$a^{(j-1)} = [a_1^{(j-1)}, \dots, a_P^{(j-1)}, \mathbf{x}^T]^T.$$

For instance, the connection between the input layer and the first hidden layer will consist of  $a^{(0)} = \mathbf{x}$ , as there are no other previous hidden nodes, and for the connection between the second-to-last and last layer,  $a^{(J-1)} = [a_1^{(J-1)}, \dots, a_P^{(J-1)}, \mathbf{x}^T]^T$  will apply.



Another difference lies in the necessity to extend the dimension of the weight matrices and inclusion parameter matrices as the covariates are concatenated, implying that more parameters will need to be considered. This contrasts with residual connections, where the previous information is simply added into succeeding nodes, which does not increase the number of parameters in the model. Inference on the models remains the same as in Hubin and Storvik [2024] and Skaaret-Lund et al. [2024] as independence is assumed between layers.

## 2.4 Active Paths

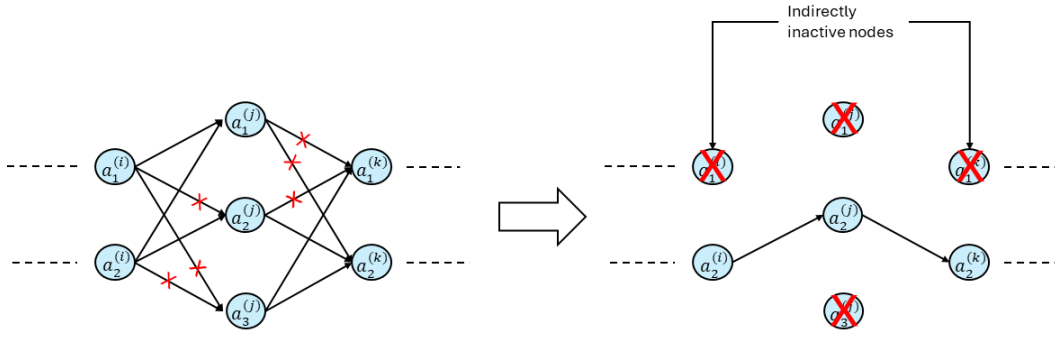


Figure 5: Example of nodes that are indirectly inactive.

Model pruning by eliminating redundant weights in neural networks, either through LBBNNs or other methods, like  $l_1$ -regularized ANNs, can lead to weights being indirectly inactive, which further deem nodes to be inactive (see Figure 5). This means that no information going into, or out of, these nodes will contribute to the prediction. With this in mind, we thus define an *active path* in a neural network as follows:

**An active path** in a neural network is a collection of adjacent weights that connects a covariate directly, or via one or more hidden nodes, to an output node.

Figure 6 illustrates active and inactive paths, emphasizing that only paths with non-zero weighted connections contribute to the prediction. This definition helps in creating sparser, more interpretable network representations by highlighting only the contributing connections. A set of all active paths in a model is further denoted as  $\mathbb{AP}$ .

It should be noted that a path that only sends information about the bias is not considered an active path. The reason for excluding these paths is twofold: Firstly, our primary interest lies in how the covariates behave, like interactions and the amount of non-linear activations needed to contribute to a prediction; Secondly, a path represented solely by bias information could be summarized in a single bias node, meaning that these connections are mainly hindering an even sparser representation of the network.

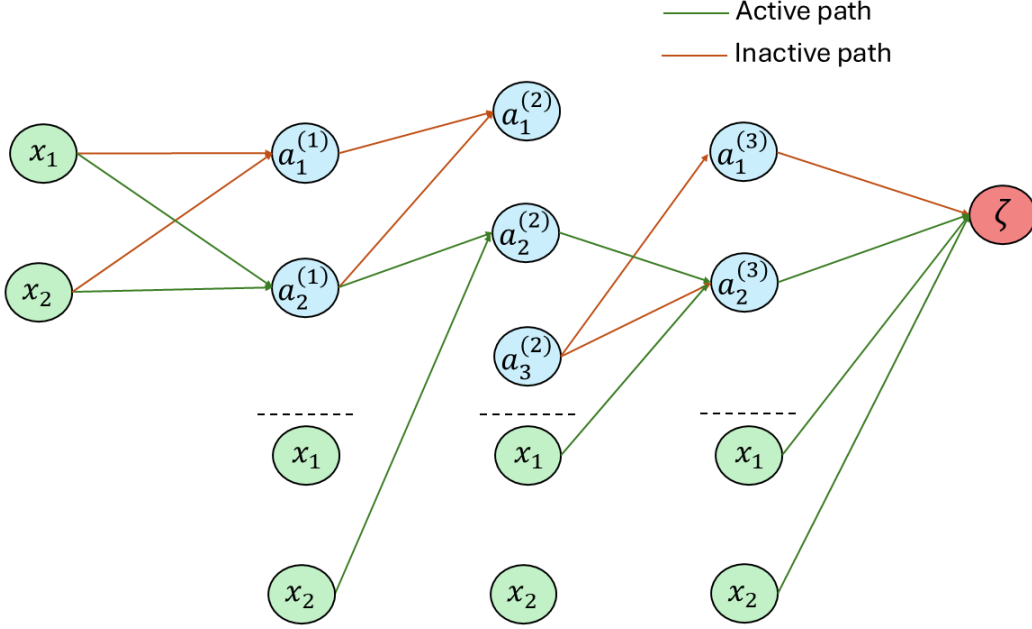


Figure 6: Examples of inactive paths after removing connections where  $\gamma = 0$  or  $w = 0$ .

## 2.5 Max and Average Depth in ISLaB Models

The ISLaB model's architecture allows covariates to skip layers, directly influencing any part of the network. This flexibility, while powerful, introduces ambiguity regarding how and where the covariates contribute to the model's predictions. In a traditional ANN without skip connections, contributions are traced from the input layer through successive layers. However, in an ISLaB model, contributions can originate from any layer, making it crucial to understand how the layers are utilized.

To gain insights into the network's behavior, it is useful to measure which layers are most frequently engaged and how many connections are required for inputs to influence the output. This can be analyzed using the concept of *contribution depth*, which we define as.

**Contribution Depth** *is the path length from a covariate (in some layer) along an active path to the output*

For instance, in a network with four hidden layers, if an active path starts from the input layer, the contribution depth would be five, as five connections are needed to reach the output.

Using this framework, we can measure the contribution depths (denoted as **depth** in the formula) for any covariate  $\mathbf{x}_i$ , where  $i = 1, 2, \dots, v$ , in an ISLaB or other relevant neural network model *from a specific layer  $j$* , represented by the following set:

$$\text{depth}(\mathbf{x}_i, j) = \bigcup_{p=1}^P \{J - j | w_{k,p}^{(j)} \in \mathbb{AP}\}. \quad (15)$$

In this equation,  $k$  corresponds to the  $i$ -th covariate in the current layer  $j$ . Thus, contributing depth shows the path length from a covariate (in some layer) along an active path to the output. This depth set can be used to derive two key metrics that describe the network’s structure: *max depth* and *average depth*.

The max depth metric is defined as the longest active path in the network:

$$\text{max depth} = \max \left( \bigcup_{j=1}^J \bigcup_{i=1}^v \text{depth}(\mathbf{x}_i, j) \right). \quad (16)$$

For example, if a covariate contributes from the input layer, the max depth would be  $J - 0 = J$ . Conversely, if the deepest contribution originates from the last hidden layer, the max depth would be  $J - (J - 1) = 1$ . Thus, max depth reflects the network’s most complex path.

To understand how deep contributions generally are within the network, we use the *average depth* metric:

$$\text{average depth} = \text{mean} \left( \bigcup_{j=1}^J \bigcup_{i=1}^v \text{depth}(\mathbf{x}_i, j) \right). \quad (17)$$

Average depth provides a general understanding of the depth of contributions across the network.

In scenarios where a network lacks active paths, the depth set is empty, resulting in both the max depth and average depth metrics being zero. This situation only occurs when the network outputs a constant prediction for all inputs, indicating no meaningful internal activity. Thus, if the covariate is not contributing to the predictions its max and average depth would be 0.

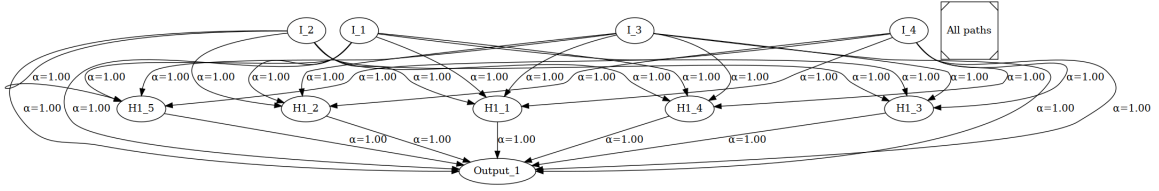
## 2.6 Global Understanding of Predictions

Interpreting the predictions of a neural network globally enhances trust in the model. Active paths facilitate a clearer understanding by focusing only on contributing weights. In LBBNNs, this can be achieved by considering active paths in the median probability model, where a weight  $w_{k,p}^{(j)}$  is included if  $\alpha_{k,p}^{(j)} > 0.5$ . Figure 7 demonstrates this concept with a simple linear problem<sup>1</sup>.

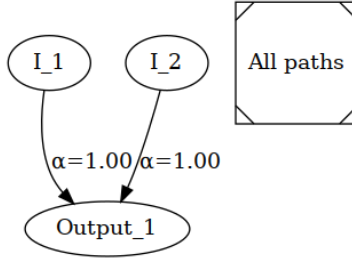
## 2.7 Local Explainability

In addition to providing global explanations, active paths allow for scalable local explanations of covariate contribution to a prediction. This is achievable by using activation functions that give linear contributions to the output layer, for instance, the ReLU activation function. Without loss of generality, we shall only consider ReLU activation in the context of local explanations. We do, however, emphasize that other piece-wise linear functions, like leaky ReLU, could give local explanations in a neural network.

1. A similar approach can be employed in  $l_1$ -regularized ANNs. However, as weights are not associated with an inclusion probability, active paths must be identified through a threshold:  $|w| > \epsilon$ ,  $\epsilon$  is typically set to a value close to zero.



(a) Full network before training.



(b) Active paths after training.

Figure 7: Before (a) and after (b) training an LRT-based ISLaB model for the linear problem  $y = x_1 + x_2 + 0x_3 + 0x_4$ .  $\alpha$  is the inclusion probability for the specific weight, where  $\alpha = 1.00$  indicates that the weight will almost surely be included in the full model. Displayed is the median probability model with its active paths. In this plot (and in similar plots to follow),  $I_1$  corresponds to the input  $x_1$ , and similarly for the other inputs, whereas  $Output\_1$  corresponds to  $y$ .

The non-linear element of the ReLU function is its capability to eliminate nodes. Elimination of nodes will simplify networks locally as weights going into, and out of, these nodes will be redundant, and the remaining network will only use linear functions to predict. This simpler, sparsified network can be used to find how much each covariate contributes to the prediction. More explicitly, by defining the set of active nodes as  $\mathbb{AN}$ , we can propagate each covariate through a network that uses Equation (18) to compute the node activations:

$$a_p^{(j)} = \mathcal{I}\left(a_p^{(j)} \in \mathbb{AN}\right) \cdot \left(\sum_{k=1}^K \mathcal{I}\left(w_{k,p}^{(j)} \in \mathbb{AP}\right) a_k^{(j-1)} w_{k,p}^{(j)}\right), \quad (18)$$

Below we shall see that the contributions conditional on a specific observation are linear.

**Proposition 1.** *Let the linear predictor parameter  $\zeta(\mathbf{x}_i)$  of the probability distribution of the responses be modeled by a neural network model with a fixed architecture and ReLU activations, parameterized by known weights  $\mathbf{W}$ . Assume with no loss of generality  $y_i \in \mathbb{R}$ . Then, conditionally on a data sample  $\mathbf{x}_i \in \mathbb{R}^v$ ,  $\zeta(\mathbf{x}_i)$  is linear in its effective input contributions and can be represented as a generalized linear model (GLM) with interpretable slope coefficients  $\beta_j$  within the linear predictor. Specifically, the model output can be expressed as:*

$$\zeta(\mathbf{x}_i) = \beta_0 + \sum_{j=1}^v \beta_j x_{ij},$$

where  $\beta_j \in \mathbb{R}$  are effective, explainable slope coefficients derived from  $\mathbf{W}$  and  $\beta_0 \in \mathbb{R}$  is an intercept term.

*Proof.* ReLU activation, defined as  $\text{ReLU}(z) = \max(0, z)$ , outputs either  $z$  if  $z > 0$  (active) or 0 otherwise (inactive). For a fixed input  $\mathbf{x}_i$  and conditional on the known architecture of the model, the binary nature of ReLU activation induces a specific pattern of active paths through the network.

Thus, conditioned on  $\mathbf{x}_i$ , the set of active neurons remains fixed, effectively reducing each layer's transformation to a linear mapping along the active paths. Further, a composition of linear mappings remains a linear mapping. Therefore,  $\zeta(\mathbf{x}_i)$  can be expressed as a weighted sum:

$$\zeta(\mathbf{x}_i) = \beta_0 + \sum_{j=1}^v \beta_j x_{ij},$$

where  $\beta_j$  are effective coefficients derived from the compositions along active path weights  $w$  across layers, and  $\beta_0$  is the cumulative intercept from these paths. This form aligns with that of a GLM, where  $\beta_j$  serves as an interpretable slope coefficient for each covariate  $x_{ij}$ .  $\square$

**Remark 1.** *This result demonstrates that neural networks with ReLU activations exhibit conditional linearity on any fixed input  $\mathbf{x}_i$ , allowing them to be interpreted as generalized linear models with parameters  $\beta$ .*

**Remark 2.** *The result holds for any piecewise-linear activation functions used as activations, since these functions still conditionally on  $\mathbf{x}_i$  give a composition of linear transformations, which are linear.*

**Remark 3.** *In the context of LBBNN, multiple samples from the posterior distribution of  $\mathbf{W}$  conditionally on  $\mathbf{\Gamma}$  can be used to generate a distribution over the slope coefficients  $\beta_i$  and intercept  $\beta_0$  for the local explanation around  $\mathbf{x}_i$ . This provides uncertainty estimates for each of these coefficients directly through the credible intervals, allowing a more comprehensive interpretation of the model’s behavior in the vicinity of  $\mathbf{x}_i$  out of the box.*

**Corollary 1.** *For a neural network with ReLU activations,  $\exists \epsilon > 0$ , such that inside the  $\epsilon$ -ball around  $\mathbf{x}_i$ , the coefficients of the LIME linear explanation based on  $n \rightarrow \infty$  random samples and their predictions based on  $\epsilon$ -ball around  $\mathbf{x}_i$  converge in probability to those  $\beta$  derived in Proposition 1 from linear explanations  $\zeta(\mathbf{x}_i) = \beta_0 + \sum_{j=1}^v \beta_j x_{ij}$ .*

*Proof.* LIME approximates the model’s behavior around a point  $\mathbf{x}_i$  by training a local linear model with a maximum likelihood method based on samples from within an  $\epsilon$ -ball around  $\mathbf{x}_i$ . In a ReLU neural network, conditional linearity (shown in Proposition 1) implies that for any fixed input  $\mathbf{x}_i$ , the model behaves as a GLM within the neighborhood defined by a small enough  $\epsilon$ -ball, within which the pattern of active neurons does not change.

Since ReLU activations partition the input space into polytopes where the model is linear within each region, any small perturbation within an  $\epsilon$ -ball around  $\mathbf{x}_i$  keeps the activation pattern fixed. Consequently, the true coefficients  $\beta_j$  and  $\beta_0$  do not vary within this  $\epsilon$ -ball, making the local linear model derived in Proposition 1 provide the coefficients to which the LIME explanation coefficients converge in probability, due to consistency of maximum likelihood estimators.  $\square$

**Remark 4.** *Unlike LIME explanations, those obtained from Proposition 1 do not require retraining for every prediction  $\mathbf{x}_i$ , and within LBBNN introduce additionally uncertainty in the parameter estimates.*

In the LBBNN setting, it will also be feasible to compute credibility intervals for covariate contributions, providing insights into the magnitude and certainty of each covariate’s impact. Figure 8 exemplifies this local explanation for a prediction made from an LBBNN model.

### 2.7.1 LOCAL EXPLAINABILITY THROUGH GRADIENTS

By Proposition 1, it becomes clear that the underlying prediction is a linear function when the activation functions are set to be piecewise linear. This realization makes it easier to find the slope coefficients,  $\beta$ , as we can simply compute the gradient directly from the neural network.

**Corollary 2.** *Let  $\mathbf{x}_i$  and  $\zeta(\mathbf{x}_i)$  be as in Proposition 1 with piecewise linear activation functions. The explanation for a prediction of an observation  $\mathbf{x}_i$  can then be found as follows:*

$$\beta = \nabla_{\mathbf{x}_i} \zeta(\mathbf{x}_i), \quad (19)$$

where  $\beta \in \mathbb{R}^v$ .

*Proof.* As shown in Proposition 1, we have that

$$\zeta(\mathbf{x}_i) = \beta_0 + \sum_{j=1}^v \beta_j x_{ij}$$

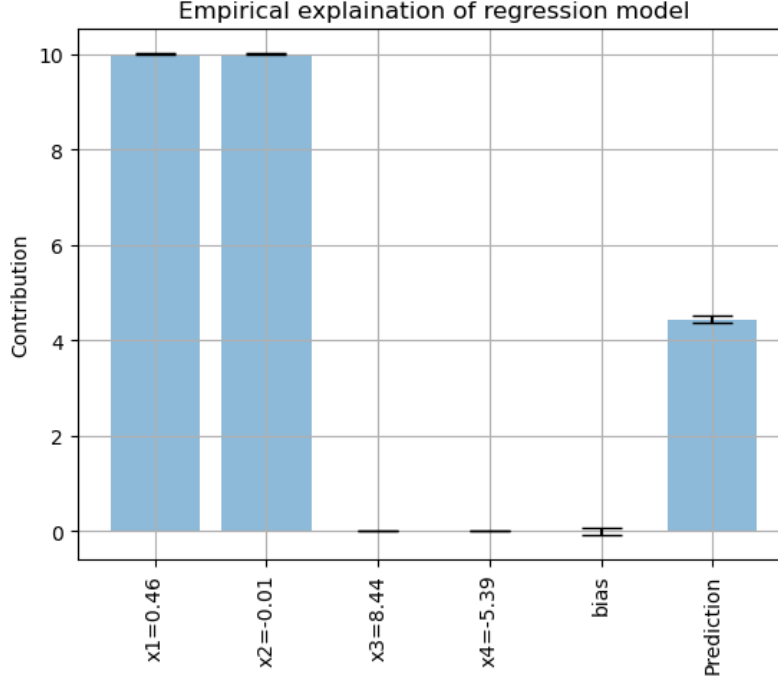


Figure 8: Local explanation for a prediction made on an LBBNN model trained on the linear problem  $y = 10x_1 + 10x_2 + 0x_3 + 0x_4$ .

holds. Therefore, by taking the gradient of  $\zeta(\cdot)$  with respect to  $\mathbf{x}_i$ , we will get  $\beta$ , which are the explainable slope coefficients.  $\square$

When explaining a prediction, we are typically interested in how much each individual covariate contributes to the given prediction. Hence, we will only consider slope coefficients where  $x_{ij} \neq 0$  in later sections (see Section 2.7). This means that

$$\beta_j = \begin{cases} \nabla_{x_{ij}} \zeta(\mathbf{x}_i), & x_{ij} \neq 0 \\ 0, & \text{otherwise} \end{cases}$$

will give the local explanation for a given prediction.

It should be mentioned that, although similar to Corollary 2 gradient-based approaches have been utilized in different forms before to give local explanations of predictions [Shrikumar et al., 2016, 2017], to the best of our knowledge it has never been seen in context to Proposition 1. That is, the explainable slope coefficients are equivalent to the ones used to produce the linear prediction for a given input. This can be directly obtained by computing the gradients with respect to the covariates, as long as piecewise linear activation functions are utilized.

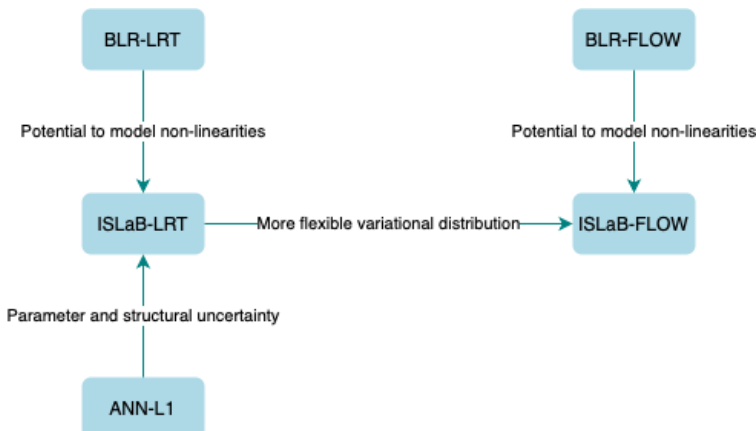


Figure 9: Illustration of the relations between the different methods considered for the experiments. Exactly one change in design is present for each edge allowing for a fully transparent ablation with clear treatments.

### 3. Experiments

#### 3.1 Experimental set-up

In the design of experiments, we want to have clear ablation rather than comparing fundamentally different entities. Thus, we benchmark our proposed ISLaB method against its closest related baseline methods. When we use the mean-field posterior, we denote it ISLaB-LRT, and ISLaB-FLOW when we in addition use normalizing flows. For the baselines, we use a simple Bayesian linear model with covariate selection, corresponding to a special case of LBBNN with only one neuron. Here, we also report results with the mean-field posterior (denoted BLR-LRT) and with normalizing flows (denoted BLR-FLOW). Lastly, we compare to a frequentist neural network, with L1 regularization on the weights, and input-skip (denoted IS-ANN-L1), representing a frequentist counterpart to our ISLaB method. For a graphical illustration of how the methods are related, see Figure 9. There direct treatment effects are introduced on each edge.

To measure performance we consider a variety of metrics that allow to evaluate methods from different perspectives. For the classification problems, we report accuracy, denoted "ACC full" when we are using all the weights, and "ACC sparse" when we are using the sparsified networks. For the ISLaB and BLR methods, the sparse networks are obtained using the median probability model (MPM) [Barbieri and Berger \[2004\]](#), i.e. removing the weights with a corresponding posterior inclusion probability less than 0.5. For the frequentist approach, we obtain the sparse results by only using the parameters that are left after removing the ones falling below a pre-determined threshold of 0.005 on weights, for all experiments. For the regression problem, we report the Pearson correlation, and root mean squared error, denoted "CORR" and "RMSE" respectively. Furthermore, we separate the dataset into two different parts when using the ISLaB models. We use a training set to learn the appropriate model parameters for the specific problem at hand, and a test set which is used to report the model performance post-training.



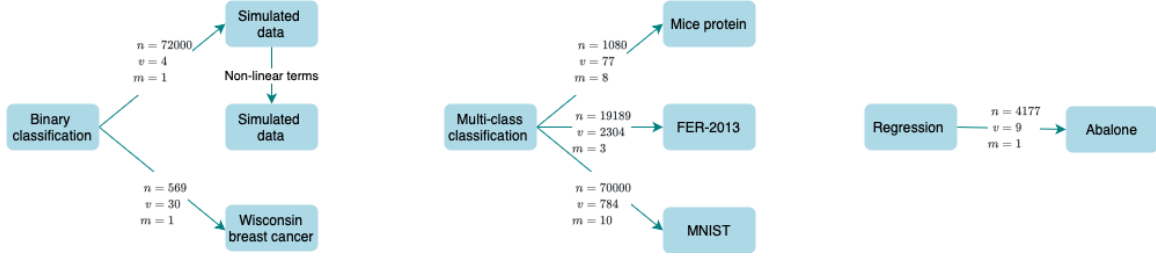


Figure 10: Datasets used in the experiments, where  $n$  denotes the number of samples,  $v$  the number of covariates, and  $m$  the number of output neurons.

Additionally, we are interested in checking what kind of structure our networks have, and how sparse they are. For this, we measure the number of weights in active paths after sparsifying the networks, denoted "Used weights". We also report the average depth ("Avg depth") and max depth ("Max depth") of the networks.

Finally, to check the calibration of the predictions, we consider two metrics. First, the expected calibration error (ECE) [Guo et al., 2017], which estimates how well the model predictions match the true probabilities, and secondly the negative test log-likelihood. For the regression problem, we report the pinball loss [Chung et al., 2021] instead of ECE.

To assess and compare our methods, we use both synthetic and real-world datasets. For an overview, we refer to Figure 10. To account for random variability, for all experiments, we run the different methods ten times and then report minimum, median, and maximum results. All hyperparameters and settings used for these experiments can be found in Table 18, while initialization for inclusion probabilities can be found in Table 17. All networks will be trained using the logistic function, also known as the sigmoid function, as the activation function for all hidden nodes.

### 3.2 Global explanations and model performance

In the first section, we start with a synthetic dataset to illustrate how our method performs with different levels of correlations, first with linear, and then non-linear data. We also check how well our method does at picking out the correct data-generating covariates. Following this, we compare results on real-world datasets. Additionally, we explore global explanations on these datasets i.e. checking which variables are influencing predictions in general. All experiments can be found and reproduced from <https://github.com/eirihoyh/ISLaB-LBBNN>.

#### 3.2.1 SIMULATED LINEAR DATA

At first, we explore two toy examples to demonstrate how the models perform when the underlying structure of the data is known. In the first example,  $\mathbf{X} = [\mathbf{x}_1, \mathbf{x}_2, \mathbf{x}_3, \mathbf{x}_4]$ , will be sampled independently from uniform distributions, spanning from  $-10$  to  $10$ . Additionally,  $\mathbf{x}_3$  will be made gradually more dependent on  $\mathbf{x}_1$  through the following equation:

$$\mathbf{x}_3 \leftarrow \varrho \cdot \mathbf{x}_1 + (1 - \varrho) \cdot \mathbf{x}_3, \quad (20)$$

where the dependence is varied over the set of values  $\varrho = \{0.0, 0.1, 0.5, 0.9\}$ . However, only  $\mathbf{x}_1$  and  $\mathbf{x}_2$  will be used as data generative covariates, which means that both  $\mathbf{x}_3$  and  $\mathbf{x}_4$  are redundant covariates and should be ignored when making decisions. We thus have:

$$\eta(\mathbf{X}) = w_0 + w_1 \mathbf{x}_1 + w_2 \mathbf{x}_2 + \epsilon, \quad (21)$$

with  $w_0 = 100$ ,  $w_1 = w_2 = 1$  and  $\epsilon_i \sim \mathcal{N}(0, 0.01^2)$ .

The problem will be transformed into a classification problem by forcing the output to be either 0 or 1 using the following equation:

$$\mathbf{y} = \begin{cases} 0, & \eta(\mathbf{X}) < \text{median}(\eta(\mathbf{X})) \\ 1, & \eta(\mathbf{X}) \geq \text{median}(\eta(\mathbf{X})). \end{cases} \quad (22)$$

We use 64000 samples for training, and 8000 for testing the trained model. For the neural network models, 4 hidden layers, each having 20 hidden nodes, will be initialized, resulting in 1544 weights initialized. The results are in Tables 1, 2, and 3.

Table 1: Results from problem described in Equation (21). The neural networks have 1544 weights, while the linear methods have 4. We report median (min, max) for all measures.

Linear problem: $\mathbf{y} = \mathbf{x}_1 + \mathbf{x}_2 + 100$					
Model; $\varrho$	ACC full	ACC sparse	Used weights	Avg depth	Max depth
ISLaB-LRT; 0.0	99.9 (99.9, 100)%	99.9 (99.9, 100)%	2 (2, 2)	1.0 (1.0, 1.0)	1 (1, 1)
ISLaB-LRT; 0.1	99.9 (99.9, 99.9)%	99.9 (99.9, 100)%	2 (2, 2)	1.0 (1.0, 1.0)	1 (1, 1)
ISLaB-LRT; 0.5	99.9 (99.9, 100)%	99.9 (99.9, 100)%	2 (2, 2)	1.0 (1.0, 1.0)	1 (1, 1)
ISLaB-LRT; 0.9	99.9 (99.9, 99.9)%	99.9 (99.9, 100)%	3 (3, 3)	1.0 (1.0, 1.0)	1 (1, 1)
ISLaB-FLOW; 0.0	99.9 (99.8, 100)%	99.9 (99.8, 99.9)%	2 (2, 2)	1.0 (1.0, 1.0)	1 (1, 1)
ISLaB-FLOW; 0.1	99.9 (99.9, 100)%	99.9 (99.8, 100)%	2 (2, 2)	1.0 (1.0, 1.0)	1 (1, 1)
ISLaB-FLOW; 0.5	99.9 (99.8, 99.9)%	99.9 (99.7, 100)%	3 (3, 3)	1.0 (1.0, 1.0)	1 (1, 1)
ISLaB-FLOW; 0.9	99.9 (99.8, 99.9)%	99.9 (99.8, 99.9)%	3 (3, 3)	1.0 (1.0, 1.0)	1 (1, 1)
BLR-LRT; 0.0	99.9 (99.9, 99.9)%	99.9 (99.9, 99.9)%	2 (2, 2)	1 (-,-)	1 (-,-)
BLR-LRT; 0.1	99.9 (99.9, 99.9)%	99.9 (99.9, 99.9)%	2 (2, 2)	1 (-,-)	1 (-,-)
BLR-LRT; 0.5	99.9 (99.9, 99.9)%	99.9 (99.9, 99.9)%	2 (2, 2)	1 (-,-)	1 (-,-)
BLR-LRT; 0.9	99.9 (99.9, 99.9)%	99.9 (99.9, 99.9)%	3 (3, 3)	1 (-,-)	1 (-,-)
BLR-FLOW; 0.0	99.9 (99.7, 99.9)%	99.9 (99.7, 99.9)%	2 (2, 2)	1 (-,-)	1 (-,-)
BLR-FLOW; 0.1	99.9 (99.7, 99.9)%	99.9 (99.7, 100)%	2 (2, 2)	1 (-,-)	1 (-,-)
BLR-FLOW; 0.5	99.9 (99.7, 99.9)%	99.9 (99.7, 99.9)%	2 (2, 2)	1 (-,-)	1 (-,-)
BLR-FLOW; 0.9	99.9 (99.8, 99.9)%	99.9 (99.8, 100)%	3 (2, 3)	1 (-,-)	1 (-,-)
IS-ANN-L1; 0.0	99.9 (99.9, 99.9)%	99.9 (99.9, 100)%	8 (5, 8)	1.7 (1.5, 1.7)	2 (2, 2)
IS-ANN-L1; 0.1	99.9 (99.9, 99.9)%	99.9 (99.9, 100)%	8 (8, 8)	1.7 (1.7, 1.7)	2 (2, 2)
IS-ANN-L1; 0.5	99.9 (99.9, 99.9)%	99.9 (99.9, 100)%	8 (8, 8)	1.7 (1.7, 1.7)	2 (2, 2)
IS-ANN-L1; 0.9	99.9 (99.9, 99.9)%	99.9 (99.9, 99.9)%	9 (9, 10)	1.7 (1.7, 1.8)	2 (2, 2)

Table 2: Expected calibration error and NLL on simulated linear data (lower is better).

Linear problem: $\mathbf{y} = \mathbf{x}_1 + \mathbf{x}_2 + 100$				
Model; $\varrho$	ECE	ECE sparse	NLL	NLL sparse
ISLaB-LRT; 0.0	0.004 (0.003, 0.004)	0.004 (0.003, 0.004)	0.005 (0.005, 0.006)	0.005 (0.005, 0.006)
ISLaB-LRT; 0.1	0.004 (0.003, 0.004)	0.004 (0.003, 0.004)	0.005 (0.005, 0.006)	0.005 (0.005, 0.006)
ISLaB-LRT; 0.5	0.004 (0.003, 0.004)	0.004 (0.003, 0.004)	0.005 (0.005, 0.006)	0.005 (0.005, 0.006)
ISLaB-LRT; 0.9	0.004 (0.003, 0.004)	0.004 (0.003, 0.004)	0.005 (0.005, 0.006)	0.005 (0.005, 0.006)
ISLaB-FLOW; 0.0	0.007 (0.006, 0.008)	0.007 (0.006, 0.008)	0.010 (0.010, 0.011)	0.010 (0.010, 0.011)
ISLaB-FLOW; 0.1	0.008 (0.007, 0.008)	0.007 (0.007, 0.008)	0.010 (0.010, 0.011)	0.010 (0.010, 0.011)
ISLaB-FLOW; 0.5	0.007 (0.006, 0.008)	0.007 (0.006, 0.008)	0.009 (0.009, 0.010)	0.009 (0.009, 0.010)
ISLaB-FLOW; 0.9	0.006 (0.005, 0.006)	0.006 (0.005, 0.006)	0.009 (0.008, 0.009)	0.009 (0.008, 0.009)
BLR-LRT; 0.0	0.007 (0.007, 0.007)	0.007 (0.006, 0.007)	0.009 (0.009, 0.009)	0.009 (0.009, 0.009)
BLR-LRT; 0.1	0.007 (0.007, 0.007)	0.007 (0.006, 0.007)	0.009 (0.009, 0.009)	0.009 (0.009, 0.009)
BLR-LRT; 0.5	0.007 (0.006, 0.007)	0.007 (0.006, 0.007)	0.009 (0.009, 0.009)	0.009 (0.009, 0.009)
BLR-LRT; 0.9	0.007 (0.006, 0.007)	0.007 (0.006, 0.007)	0.009 (0.009, 0.009)	0.009 (0.009, 0.009)
BLR-FLOW; 0.0	0.002 (0.001, 0.002)	0.002 (0.001, 0.003)	0.004 (0.003, 0.006)	0.004 (0.003, 0.006)
BLR-FLOW; 0.1	0.002 (0.001, 0.002)	0.002 (0.001, 0.002)	0.004 (0.003, 0.005)	0.004 (0.003, 0.005)
BLR-FLOW; 0.5	0.002 (0.001, 0.002)	0.002 (0.001, 0.002)	0.004 (0.003, 0.006)	0.004 (0.003, 0.006)
BLR-FLOW; 0.9	0.002 (0.001, 0.003)	0.002 (0.001, 0.003)	0.004 (0.003, 0.005)	0.004 (0.003, 0.005)
IS-ANN-L1; 0.0	0.007 (0.007, 0.007)	0.007 (0.007, 0.007)	0.009 (0.009, 0.009)	0.009 (0.009, 0.009)
IS-ANN-L1; 0.1	0.007 (0.007, 0.007)	0.007 (0.007, 0.007)	0.009 (0.009, 0.010)	0.009 (0.009, 0.009)
IS-ANN-L1; 0.5	0.007 (0.007, 0.007)	0.007 (0.007, 0.008)	0.009 (0.009, 0.010)	0.009 (0.009, 0.010)
IS-ANN-L1; 0.9	0.007 (0.007, 0.007)	0.007 (0.007, 0.007)	0.009 (0.009, 0.009)	0.009 (0.009, 0.009)

Table 3: Same methods as used in Table 1. Here, the inclusion rates are reported for each covariate that is fed into the model.

Linear problem: $\mathbf{y} = \mathbf{x}_1 + \mathbf{x}_2 + 100$				
Model; $\varrho$	Inclusion rate $\mathbf{x}_1$	Inclusion rate $\mathbf{x}_2$	Inclusion rate $\mathbf{x}_3$	Inclusion rate $\mathbf{x}_4$
ISLaB-LRT; 0.0	100%	100%	0%	0%
ISLaB-LRT; 0.1	100%	100%	0%	0%
ISLaB-LRT; 0.5	100%	100%	0%	0%
ISLaB-LRT; 0.9	100%	100%	100%	0%
ISLaB-FLOW; 0.0	100%	100%	0%	0%
ISLaB-FLOW; 0.1	100%	100%	0%	0%
ISLaB-FLOW; 0.5	100%	100%	100%	0%
ISLaB-FLOW; 0.9	100%	100%	100%	0%
BLR-LRT; 0.0	100%	100%	0%	0%
BLR-LRT; 0.1	100%	100%	0%	0%
BLR-LRT; 0.5	100%	100%	0%	0%
BLR-LRT; 0.9	100%	100%	100%	0%
BLR-FLOW; 0.0	100%	100%	0%	0%
BLR-FLOW; 0.1	100%	100%	0%	0%
BLR-FLOW; 0.5	100%	100%	0%	0%
BLR-FLOW; 0.9	100%	100%	80%	0%
IS-ANN-L1; 0.0	100%	100%	0%	0%
IS-ANN-L1; 0.1	100%	100%	0%	0%
IS-ANN-L1; 0.5	100%	100%	0%	0%
IS-ANN-L1; 0.9	100%	100%	100%	0%

The results indicate that all methods perform well with and without sparsification, with close to 100% accuracy. This is perhaps not surprising as this is a very simple linear problem. From Table 3 we can see that all methods include  $x_3$  with high correlation. We note that our methods typically do very well at pruning away all the irrelevant (of 1544) weights and only use the two linear terms, where an example of the typical learned structure is presented

in Figure 11. This behavior is not seen in IS-ANN-L1, as it uses around 8 weights. For the calibration, ISLaB-LRT has lower ECE and NLL than the frequentist approach and ISLaB-FLOW, whereas the latter two are similar. Overall, the linear method BLR-FLOW has the best results here, which is perhaps not surprising as we know that the data generative process is linear.

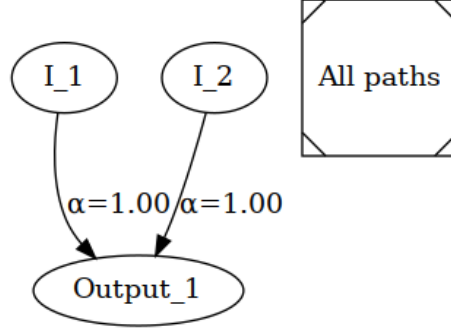


Figure 11: Typical learned structures of Equation (21) when using  $\varrho = 0.0$  for an FLOW-based model.  $\alpha$  indicates the inclusion probability and displayed is the median probability model with its active paths. Such graphs allow for transparent global explanations based on our models showing significant paths for each selected covariate (both in terms of MPM).

### 3.2.2 SIMULATED NON-LINEAR DATA

The setup in this experiment is the same as in the previous section, however here we add an interaction term and squared covariates:

$$\eta(\mathbf{X}) = w_0 + w_1 \mathbf{x}_1 + w_2 \mathbf{x}_2 + w_3 \mathbf{x}_1 \mathbf{x}_2 + w_4 \mathbf{x}_1^2 + w_5 \mathbf{x}_2^2 + \epsilon, \quad (23)$$

with  $w_3 = w_4 = w_5 = 1$ . The results can be found in Table 4, 5, and 6.

Table 4: Results from problem described in Equation (23). See Table 1 for more information.

Non-linear problem: $\mathbf{y} = \mathbf{x}_1 + \mathbf{x}_2 + \mathbf{x}_1\mathbf{x}_2 + \mathbf{x}_1^2 + \mathbf{x}_2^2 + 100$					
Model; $\rho$	ACC full	ACC sparse	Used weights	Avg depth	Max depth
ISLaB-LRT; 0.0	99.8 (99.7, 99.9)%	99.8 (99.7, 99.9)%	45.0 (25, 74)	2.33 (2.23, 2.63)	3.0 (3, 4)
ISLaB-LRT; 0.1	99.8 (99.4, 99.9)%	99.8 (99.4, 99.9)%	45.0 (16, 63)	2.33 (2.22, 2.54)	3.0 (3, 4)
ISLaB-LRT; 0.5	99.8 (99.6, 99.9)%	99.8 (99.7, 99.9)%	47.5 (38, 71)	2.30 (2.13, 2.56)	3.0 (3, 4)
ISLaB-LRT; 0.9	99.7 (99.4, 99.8)%	99.7 (99.4, 99.8)%	60.5 (33, 74)	2.32 (2.22, 2.47)	3.5 (3, 4)
ISLaB-FLOW; 0.0	99.8 (99.6, 99.8)%	99.8 (99.7, 99.8)%	70.5 (18, 109)	2.46 (2.00, 2.67)	4.0 (3, 5)
ISLaB-FLOW; 0.1	99.8 (99.1, 99.9)%	99.8 (99.1, 99.9)%	70.0 (14, 107)	2.56 (2.00, 2.73)	4.5 (3, 5)
ISLaB-FLOW; 0.5	99.8 (99.7, 99.9)%	99.8 (99.7, 99.9)%	84.5 (59, 113)	2.60 (2.20, 2.83)	4.0 (3, 5)
ISLaB-FLOW; 0.9	99.8 (99.7, 99.8)%	99.8 (99.7, 99.9)%	85.0 (38, 125)	2.45 (2.00, 2.61)	4.0 (3, 5)
BLR-LRT; 0.0	55.5 (55.3, 55.5)%	55.4 (55.0, 56.0)%	2 (2, 2)	1 (-,-)	1 (-,-)
BLR-LRT; 0.1	55.5 (55.3, 55.5)%	55.4 (55.0, 56.0)%	2 (2, 2)	1 (-,-)	1 (-,-)
BLR-LRT; 0.5	55.5 (55.3, 55.5)%	55.4 (55.0, 56.0)%	2 (2, 2)	1 (-,-)	1 (-,-)
BLR-LRT; 0.9	55.6 (55.4, 55.8)%	55.6 (55.0, 56.1)%	2 (2, 2)	1 (-,-)	1 (-,-)
BLR-FLOW; 0.0	55.6 (55.4, 55.9)%	55.8 (55.1, 55.9)%	2 (2, 2)	1 (-,-)	1 (-,-)
BLR-FLOW; 0.1	55.6 (55.5, 56.0)%	55.7 (55.3, 56.0)%	2 (2, 2)	1 (-,-)	1 (-,-)
BLR-FLOW; 0.5	55.6 (55.4, 55.9)%	55.7 (55.4, 55.9)%	2 (2, 2)	1 (-,-)	1 (-,-)
BLR-FLOW; 0.9	55.9 (55.5, 55.9)%	55.7 (55.0, 56.0)%	2 (2, 2)	1 (-,-)	1 (-,-)
IS-ANN-L1; 0.0	99.3 (98.8, 99.6)%	99.3 (98.8, 99.6)%	31.5 (16, 40)	2.30 (2.13, 2.40)	3 (3, 3)
IS-ANN-L1; 0.1	99.1 (97.8, 99.5)%	99.1 (97.8, 99.5)%	31.0 (27, 35)	2.20 (1.73, 2.38)	3 (2, 3)
IS-ANN-L1; 0.5	99.4 (97.8, 99.6)%	99.4 (97.8, 99.6)%	30.0 (12, 44)	2.27 (1.67, 2.35)	3 (2, 3)
IS-ANN-L1; 0.9	99.5 (98.8, 99.7)%	99.4 (98.8, 99.7)%	36.5 (26, 43)	2.31 (2.06, 2.38)	3 (3, 3)

Table 5: Expected calibration error and NLL on simulated non-linear data (lower is better).

Non-linear problem: $\mathbf{y} = \mathbf{x}_1 + \mathbf{x}_2 + \mathbf{x}_1\mathbf{x}_2 + \mathbf{x}_1^2 + \mathbf{x}_2^2 + 100$				
Model; $\rho$	ECE	ECE sparse	NLL	NLL sparse
ISLaB-LRT; 0.0	0.004 (0.003, 0.009)	0.004 (0.003, 0.009)	0.009 (0.005, 0.015)	0.009 (0.005, 0.015)
ISLaB-LRT; 0.1	0.005 (0.003, 0.012)	0.004 (0.003, 0.012)	0.009 (0.006, 0.024)	0.009 (0.006, 0.024)
ISLaB-LRT; 0.5	0.005 (0.003, 0.007)	0.005 (0.003, 0.007)	0.009 (0.006, 0.012)	0.009 (0.006, 0.012)
ISLaB-LRT; 0.9	0.004 (0.003, 0.011)	0.004 (0.003, 0.012)	0.009 (0.007, 0.020)	0.009 (0.007, 0.020)
ISLaB-FLOW; 0.0	0.004 (0.003, 0.009)	0.004 (0.003, 0.009)	0.008 (0.007, 0.016)	0.008 (0.007, 0.016)
ISLaB-FLOW; 0.1	0.004 (0.003, 0.011)	0.004 (0.003, 0.011)	0.008 (0.006, 0.026)	0.008 (0.006, 0.026)
ISLaB-FLOW; 0.5	0.004 (0.002, 0.008)	0.004 (0.002, 0.008)	0.007 (0.006, 0.014)	0.007 (0.006, 0.014)
ISLaB-FLOW; 0.9	0.004 (0.003, 0.008)	0.004 (0.003, 0.008)	0.008 (0.007, 0.014)	0.008 (0.007, 0.014)
BLR-LRT; 0.0	0.024 (0.023, 0.025)	0.024 (0.020, 0.029)	0.689 (0.689, 0.689)	0.689 (0.689, 0.689)
BLR-LRT; 0.1	0.025 (0.023, 0.025)	0.024 (0.020, 0.029)	0.689 (0.689, 0.689)	0.689 (0.689, 0.689)
BLR-LRT; 0.5	0.025 (0.023, 0.025)	0.024 (0.020, 0.029)	0.689 (0.689, 0.689)	0.689 (0.689, 0.689)
BLR-LRT; 0.9	0.025 (0.024, 0.027)	0.025 (0.020, 0.031)	0.689 (0.688, 0.689)	0.689 (0.688, 0.689)
BLR-FLOW; 0.0	0.023 (0.020, 0.036)	0.024 (0.017, 0.033)	0.689 (0.688, 0.690)	0.689 (0.688, 0.690)
BLR-FLOW; 0.1	0.020 (0.019, 0.025)	0.022 (0.017, 0.025)	0.688 (0.688, 0.689)	0.688 (0.688, 0.689)
BLR-FLOW; 0.5	0.020 (0.019, 0.024)	0.021 (0.017, 0.026)	0.688 (0.688, 0.689)	0.688 (0.688, 0.689)
BLR-FLOW; 0.9	0.022 (0.020, 0.024)	0.022 (0.017, 0.026)	0.688 (0.688, 0.689)	0.688 (0.688, 0.689)
IS-ANN-L1; 0.0	0.032 (0.028, 0.037)	0.032 (0.028, 0.037)	0.049 (0.043, 0.051)	0.048 (0.043, 0.051)
IS-ANN-L1; 0.1	0.031 (0.028, 0.060)	0.031 (0.028, 0.060)	0.049 (0.046, 0.104)	0.049 (0.046, 0.104)
IS-ANN-L1; 0.5	0.034 (0.028, 0.048)	0.034 (0.027, 0.048)	0.048 (0.043, 0.089)	0.048 (0.043, 0.089)
IS-ANN-L1; 0.9	0.035 (0.026, 0.038)	0.035 (0.026, 0.037)	0.047 (0.045, 0.052)	0.047 (0.045, 0.052)

The results indicate that our methods perform well both with the full and sparse model, with high accuracy and correctly selecting the data-generating covariates. While the linear methods are also able to do this, they have no way to model the interaction and square terms, and therefore the accuracy is poor. As illustrated in Figure 12, our method now learns a non-linear structure when presented with non-linear terms, which shows that it is able to adapt in accordance with the complexity of the problem at hand. IS-ANN-L1 has good accuracy with the full model and even sparser model, however, it has much higher ECE and NLL than our ISLaB methods, indicating significantly worse uncertainty handling. These two toy experiments indicate that our novel method can perform well in a variety

Table 6: Same models as used in Table 4. The inclusion rates of each covariate fed into the model.

Non-linear problem: $\mathbf{y} = \mathbf{x}_1 + \mathbf{x}_2 + \mathbf{x}_1\mathbf{x}_2 + \mathbf{x}_1^2 + \mathbf{x}_2^2 + 100$				
Model; $\varrho$	Inclusion rate $\mathbf{x}_1$	Inclusion rate $\mathbf{x}_2$	Inclusion rate $\mathbf{x}_3$	Inclusion rate $\mathbf{x}_4$
ISLaB-LRT; 0.0	100%	100%	0%	0%
ISLaB-LRT; 0.1	100%	100%	0%	0%
ISLaB-LRT; 0.5	100%	100%	0%	0%
ISLaB-LRT; 0.9	100%	100%	100%	0%
ISLaB-FLOW; 0.0	100%	100%	0%	0%
ISLaB-FLOW; 0.1	100%	100%	0%	0%
ISLaB-FLOW; 0.5	100%	100%	0%	0%
ISLaB-FLOW; 0.9	100%	100%	100%	0%
BLR-LRT; 0.0	100%	100%	0%	0%
BLR-LRT; 0.1	100%	100%	0%	0%
BLR-LRT; 0.5	100%	100%	0%	0%
BLR-LRT; 0.9	50%	100%	50%	0%
BLR-FLOW; 0.0	100%	100%	0%	0%
BLR-FLOW; 0.1	100%	100%	0%	0%
BLR-FLOW; 0.5	100%	100%	0%	0%
BLR-FLOW; 0.9	60%	100%	40%	0%
IS-ANN-L1; 0.0	100%	100%	0%	0%
IS-ANN-L1; 0.1	100%	100%	10%	0%
IS-ANN-L1; 0.5	100%	100%	60%	0%
IS-ANN-L1; 0.9	100%	100%	100%	0%

of settings, due to its flexibility and ability to *learn* the needed model complexity from the data, while maintaining predictive accuracy and uncertainty handling.

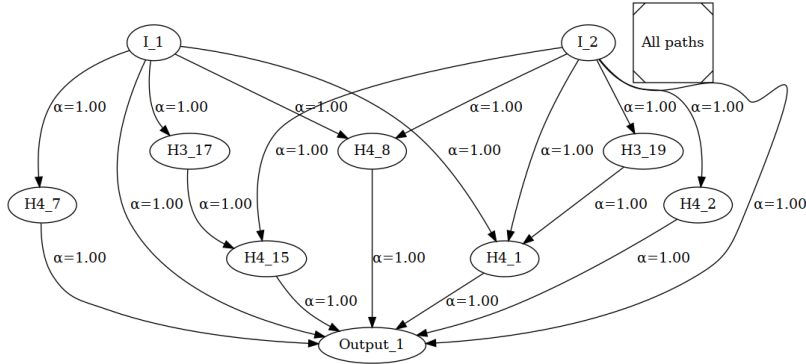


Figure 12: Sparse structure learned of Equation (23) when using  $\varrho = 0.0$  for an FLOW-based model.  $\alpha$  indicates the inclusion probability and displayed is the median probability model with its active paths.

### 3.2.3 WISCONSIN BREAST CANCER

Having established that the ISLaB method is capable of finding linear and non-linear structures when presented with simple problems where the functional form is known, the focus

will now shift to real-world datasets. The first problem to be examined is the Wisconsin breast cancer (WBC) dataset. The data is labeled as either malignant or benign and can be found in [Wolberg et al. \[1995\]](#).

The neural network methods were initiated with 2 hidden layers, each having 50 hidden nodes, resulting in 5’580 weights in the full network. All covariates will be min-max scaled such that the largest value is equal to 1 and the smallest is equal to 0. We used 512 samples for training and 57 for testing the network after training.

The metrics related to the accuracy and the number of used weights are found in Table 7, and an example of a typical ISaB model is presented in Figure 13. From Table 7 we see that all methods have high accuracies for both full and sparse networks, with our proposed method slightly lower. We also see that the linear methods use about the same number of weights as our methods (again demonstrating our method’s ability to prune away the vast majority of irrelevant covariates). Similar results were achieved in [Hubin et al. \[2021\]](#) and [Hubin et al. \[2023\]](#), where a Bayesian generalized nonlinear model and Bayesian fractional polynomial model only learned linear terms. This underscores that the true structure might indeed be linear. The frequentist network uses roughly twice the number of weights, but still only linear connections. On average the accuracies of the frequentist and Bayesian linear models are slightly higher, yet upper bounds are exactly the same for all the approaches. The results on calibration are in Table 8. Here we see that our proposed method does better than the frequentist baseline, with both lower ECE and NLL. It is also better than the linear models for the respective inference types (FLOW, LRT).

Table 7: Results from Wisconsin Breast Cancer dataset. Two hidden layers, each consisting of 50 nodes, were used. ISLaB-LRT (100) indicates that the results were computed using 100 samples from the variational posterior, while (1000) indicates that 1000 samples were used. Same with ISLaB-FLOW.

Accuracy and used weights, WBC dataset					
Model	ACC full	ACC sparse	Used weights	Avg depth	Max depth
ISLaB-LRT	96.5 (96.5, 98.2)%	96.5 (96.5, 98.2)%	4.0 (3, 6)	1.0 (1.0, 1.0)	1 (1, 1)
ISLaB-FLOW	96.5 (93.0, 98.2)%	96.5 (93.0, 98.2)%	4.5 (3, 5)	1.0 (1.0, 1.0)	1 (1, 1)
BLR-LRT	98.2 (96.5, 98.2)%	98.2 (96.5, 98.2)%	5.0 (4, 6)	1 (-,-)	1 (-,-)
BLR-FLOW	98.2 (96.5, 98.2)%	98.2 (93.0, 98.2)%	5.0 (3, 5)	1 (-,-)	1 (-,-)
IS-ANN-L1	98.2 (98.2, 98.2)%	98.2 (98.2, 98.2)%	9.5 (6, 12)	1.0 (1.0, 1.0)	1 (1, 1)

Table 8: Expected calibration error and NLL (lower is better).

Calibration and negative log-likelihood, WBC dataset				
Model	ECE full	ECE sparse	NLL full	NLL sparse
ISLaB-LRT	0.142 (0.132, 0.164)	0.146 (0.131, 0.165)	0.206 (0.192, 0.229)	0.207 (0.192, 0.230)
ISLaB-FLOW	0.153 (0.131, 0.171)	0.155 (0.136, 0.170)	0.220 (0.206, 0.248)	0.213 (0.204, 0.247)
BLR-LRT	0.153 (0.134, 0.170)	0.150 (0.139, 0.164)	0.207 (0.197, 0.227)	0.204 (0.190, 0.220)
BLR-FLOW	0.172 (0.167, 0.195)	0.171 (0.127, 0.187)	0.234 (0.222, 0.287)	0.234 (0.222, 0.287)
IS-ANN-L1	0.226 (0.219, 0.226)	0.226 (0.226, 0.227)	0.296 (0.295, 0.296)	0.296 (0.295, 0.297)

### 3.2.4 ABALONE DATASET

This dataset presents a regression task, with the objective being to accurately predict the number of rings an abalone possesses, as this serves as an indicator of its age. The data can be accessed from [Nash et al. \[1995\]](#). For this problem, the neural network-based approaches

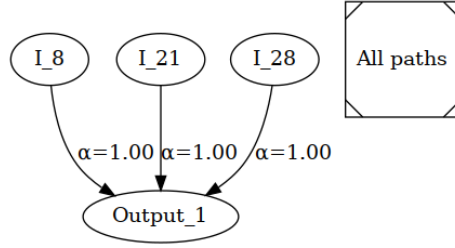


Figure 13: Typical learned structure by an ISLaB-FLOW network trained on the WBC dataset.  $\alpha$  indicates the inclusion probability in the full model.

have 2 hidden layers, each containing 200 nodes, giving 43'809 weights in the full model. The data will be partitioned into a training set with 3'759 observations, and a test set with 418 observations.

RMSE and Pinball are presented in Table 10. Here, all neural network-based methods obtain similar results, on both the RMSE and Pinball loss, however, they outperform the linear models for these metrics. ISLaB-LRT has the best overall predictions and uncertainty handling. As seen in Table 9, the ISLaB-FLOW methods obtained sparser networks than the other non-linear approaches with an example of a learned structure is shown in Figure 14. We also note again that the frequentist network uses more weights than the other approaches. It is further observed that our methods use more parameters than would be necessary for only linear terms. This is consistent with the results in Hubin et al. [2023] and Hubin et al. [2021], where their models needed non-linear components to attain accurate predictions.

Table 9: Results from the Abalone dataset. Two hidden layers, each consisting of 200 nodes, were used.

Metrics on the Abalone dataset					
Model	Corr full	Corr sparse	Used weights	Avg depth	Max depth
ISLaB-LRT	0.78 (0.78, 0.79)	0.78 (0.78, 0.79)	24.5 (17, 34)	1.62 (1.50, 1.76)	2 (2, 2)
ISLaB-FLOW	0.78 (0.75, 0.79)	0.78 (0.75, 0.79)	11.0 (6, 20)	1.33 (1.00, 1.76)	2 (1, 2)
BLR-LRT	0.74 (0.74, 0.74)	0.74 (0.74, 0.74)	9.0 (9, 9)	1 (-,-)	1 (-,-)
BLR-FLOW	0.76 (0.74, 0.76)	0.76 (0.74, 0.76)	7.0 (6, 8)	1 (-,-)	1 (-,-)
IS-ANN-L1	0.78 (0.77, 0.78)	0.78 (0.78, 0.79)	95.0 (80,104)	2.13 (2.00, 2.25)	3 (3, 3)

Table 10: Results from the Abalone dataset. Two hidden layers, each consisting of 200 nodes, were used.

RMSE and Pinball loss for the Abalone dataset				
Model	RMSE full	RMSE sparse	Pinball	Pinball sparse
ISLaB-LRT	2.08 (2.06, 2.10)	2.08 (2.06, 2.10)	0.73 (0.72, 0.74)	0.73 (0.72, 0.74)
ISLaB-FLOW	2.12 (2.07, 2.21)	2.12 (2.07, 2.21)	0.75 (0.72, 0.80)	0.75 (0.72, 0.80)
BLR-LRT	2.24 (2.24, 2.25)	2.24 (2.24, 2.25)	0.80 (0.80, 0.81)	0.80 (0.80, 0.80)
BLR-FLOW	2.19 (2.18, 2.27)	2.19 (2.18, 2.27)	0.79 (0.78, 0.82)	0.79 (0.78, 0.82)
IS-ANN-L1	2.11 (2.10, 2.12)	2.08 (2.06, 2.09)	0.78 (0.77, 0.78)	0.74 (0.73, 0.75)



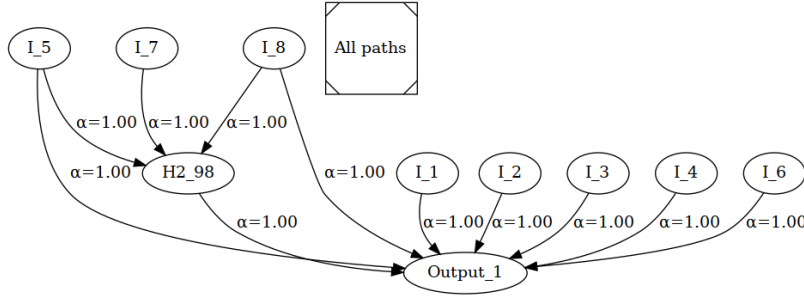


Figure 14: Typical learned structure by ISLaB-FLOW network trained on the abalone dataset.  $\alpha$  indicates the inclusion probability in the full model.

### 3.2.5 MICE PROTEIN DATASET

In the mice protein dataset from [Higuera et al. \[2015b\]](#), mice are categorized into one of 8 different classes, where the explanations for each class can be found in Table 19. For the neural network approaches, 4 hidden layers will be used, where each hidden layer has 100 hidden nodes, which gives 62’216 weights in the full model. The training set will have 972 observations, and 108 observations will be used as a test set to evaluate the performance of the trained models.

Table 11 presents the results related to the accuracy, used weights, and depth. The highest accuracy was generally attained with the IS-ANN-L1 and ISLaB-LRT methods, with ISLaB-FLOW doing slightly worse and linear models performing further worse. The results on calibration can be found in Table 12. Here we see that the linear BLR-LRT method has the lowest ECE with both the full and sparse networks, and the frequentist method has the lowest NLL.

On this dataset, the linear methods are performing quite well, and we see that the non-linear methods are mostly reduced to linear methods as well. Again we see that the frequentist approach uses a significantly larger number of weights than all other baselines. To illustrate how our methods can help with interpretability, Figure 15 shows all paths that lead to classes 1 and 5 for a FLOW-based network. This simplifies the task for researchers when choosing proteins to further investigate, as information about which proteins contribute to the different classes is available. Furthermore, since all connections are linear, it will be feasible to determine whether covariates contribute positively or negatively to a given class.

Table 11: Results from the Mice protein dataset. Four hidden layers, each consisting of 100 nodes were used.

Model (samples)	ACC and used weights, Mice protein dataset				
	ACC full	ACC sparse	Used weights	Avg depth	Max depth
ISLaB-LRT	99.1 (98.1, 100)%	99.1 (97.2, 100)%	140.0 (134, 145)	1.00 (1.00, 1.00)	1 (1, 1)
ISLaB-FLOW	97.2 (96.3, 99.1)%	97.2 (96.3, 99.1)%	98.5 (88, 111)	1.00 (1.00, 1.00)	1 (1, 1)
BLR-LRT	96.8 (96.3, 97.2)%	96.8 (96.3, 98.1)%	63.0 (60, 65)	1 (-,-)	1 (-,-)
BLR-FLOW	96.8 (94.4, 99.1)%	96.3 (94.4, 99.1)%	103.0 (85, 115)	1 (-,-)	1 (-,-)
IS-ANN-L1	99.1 (99.1, 100)%	99.1 (99.1, 100)%	214.5 (209, 234)	1.02 (1.00, 1.11)	2 (1, 2)

Table 12: Expected calibration error and NLL on Mice data. Lower is better.

Model (samples)	Ece and NLL			
	ECE full	ECE sparse	NLL	NLL sparse
ISLaB-LRT	0.072 (0.053, 0.092)	0.062 (0.032, 0.080)	0.203 (0.162, 0.238)	0.185 (0.140, 0.236)
ISLaB-FLOW	0.053 (0.042, 0.067)	0.053 (0.035, 0.067)	0.340 (0.184, 0.649)	0.318 (0.167, 0.675)
BLR-LRT	0.036 (0.017, 0.055)	0.033 (0.014, 0.050)	0.286 (0.207, 0.375)	0.278 (0.205, 0.378)
BLR-FLOW	0.057 (0.033, 0.072)	0.040 (0.050, 0.085)	0.485 (0.262, 0.860)	0.485 (0.282, 0.806)
IS-ANN-L1	0.066 (0.056, 0.068)	0.066 (0.056, 0.068)	0.079 (0.077, 0.081)	0.079 (0.077, 0.081)

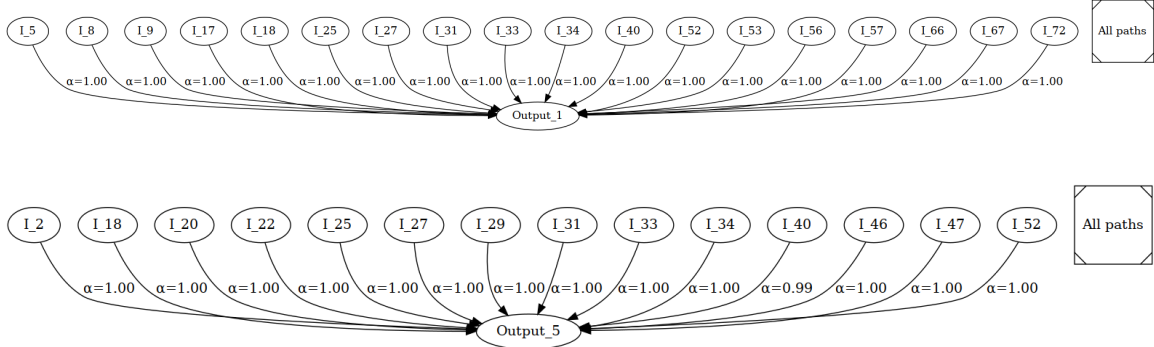


Figure 15: Typical learned structure by ISLaB-FLOW network trained on the mice protein dataset. At the top, all connections go into class 1, with connections into class 5 at the bottom.

### 3.2.6 FER2013 DATASET - HAPPY, SURPRISED AND NEUTRAL

The next example to be examined is the FER2013 image dataset, which is based on a Kaggle competition [Erhan et al., 2013]. The dataset consists of images with expressions of anger, disgust, fear, happiness, sadness, surprise, and neutrality. However, for this experiment, the focus will be on the three expressions: happy, surprised, and neutral. For the neural network-based implementations, there will be 2 hidden layers, each containing 200 hidden nodes, resulting in 969'112 weights in the full model. The network will be trained with 17'270 observations, and tested with the remaining 1'919 observations.

The obtained accuracy and the final density after training can be found in Table 13. Here, it can be seen that the frequentist approach has slightly higher accuracy than the other methods while using a lot more weights. We note that the linear methods perform quite well on this dataset. The ISLaB-based methods use even fewer weights than the linear ones, but we note that all approaches only use linear weights as can be seen in the depth metrics. The results on calibration are in Table 14, where we see similar results for all approaches.

Figure 16 illustrates the pixels used to make predictions in an ISLaB-FLOW network. A particularly interesting observation from these explanations is that the method appears to focus on the correct regions when making predictions. For instance, Figure 16a, which illustrates which pixels are used for predicting a happy facial expression, indicates that the method uses pixels around the mouth region where a smile is typically present. This seems

reasonable as it is a region that humans also focus on when determining whether a person is happy. We can also see that the input layer and the first hidden layer are redundant and do not contribute to the predictions, indicating a linear model, which explains why the linear methods have comparable to neural networks accuracy on this dataset.

Table 13: Results from FER2013 HSN dataset. Two hidden layers, each consisting of 200 nodes, were used.

Accuracy and used weights, FER2013 HSN dataset					
Model	ACC full	ACC sparse	Used weights	Avg depth	Max depth
ISLaB-LRT	59.6 (58.5, 60.6)%	59.5 (58.3, 60.4)%	24.0 (22, 28)	1.0 (1.0, 1.0)	1 (1, 1)
ISLaB-FLOW	58.4 (57.3, 59.5)%	58.3 (57.4, 59.7)%	24.0 (20, 36)	1.0 (1.0, 1.0)	1 (1, 1)
BLR-LRT	60.3 (60.0, 61.3)%	60.4 (60.1, 61.1)%	34.0 (32, 38)	1 (-,-)	1 (-,-)
BLR-FLOW	60.7 (60.3, 61.1)%	60.9 (59.9, 61.6)%	28.5 (25, 32)	1 (-,-)	1 (-,-)
IS-ANN-L1	62.3 (62.3, 62.4)%	63.9 (63.2, 64.4)%	746.5 (736, 752)	1.0 (1.0, 1.0)	1 (1, 1)

Table 14: Expected calibration error and NLL on the FER2013 HSN dataset, where lower values are better.

Model	ECE full	ECE sparse	NLL sparse	NLL full
ISLaB-LRT	0.024 (0.014, 0.046)	0.023 (0.013, 0.043)	0.882 (0.875, 0.893)	0.883 (0.875, 0.894)
ISLaB-FLOW	0.023 (0.017, 0.030)	0.022 (0.014, 0.059)	0.938 (0.921, 0.954)	0.898 (0.888, 0.919)
BLR-LRT	0.027 (0.013, 0.038)	0.029 (0.023, 0.034)	0.876 (0.873, 0.881)	0.876 (0.873, 0.883)
BLR-FLOW	0.030 (0.013, 0.035)	0.031 (0.017, 0.042)	0.881 (0.873, 0.896)	0.876 (0.867, 0.889)
IS-ANN-L1	0.025 (0.024, 0.028)	0.021 (0.012, 0.024)	0.847 (0.846, 0.847)	0.828 (0.828, 0.829)

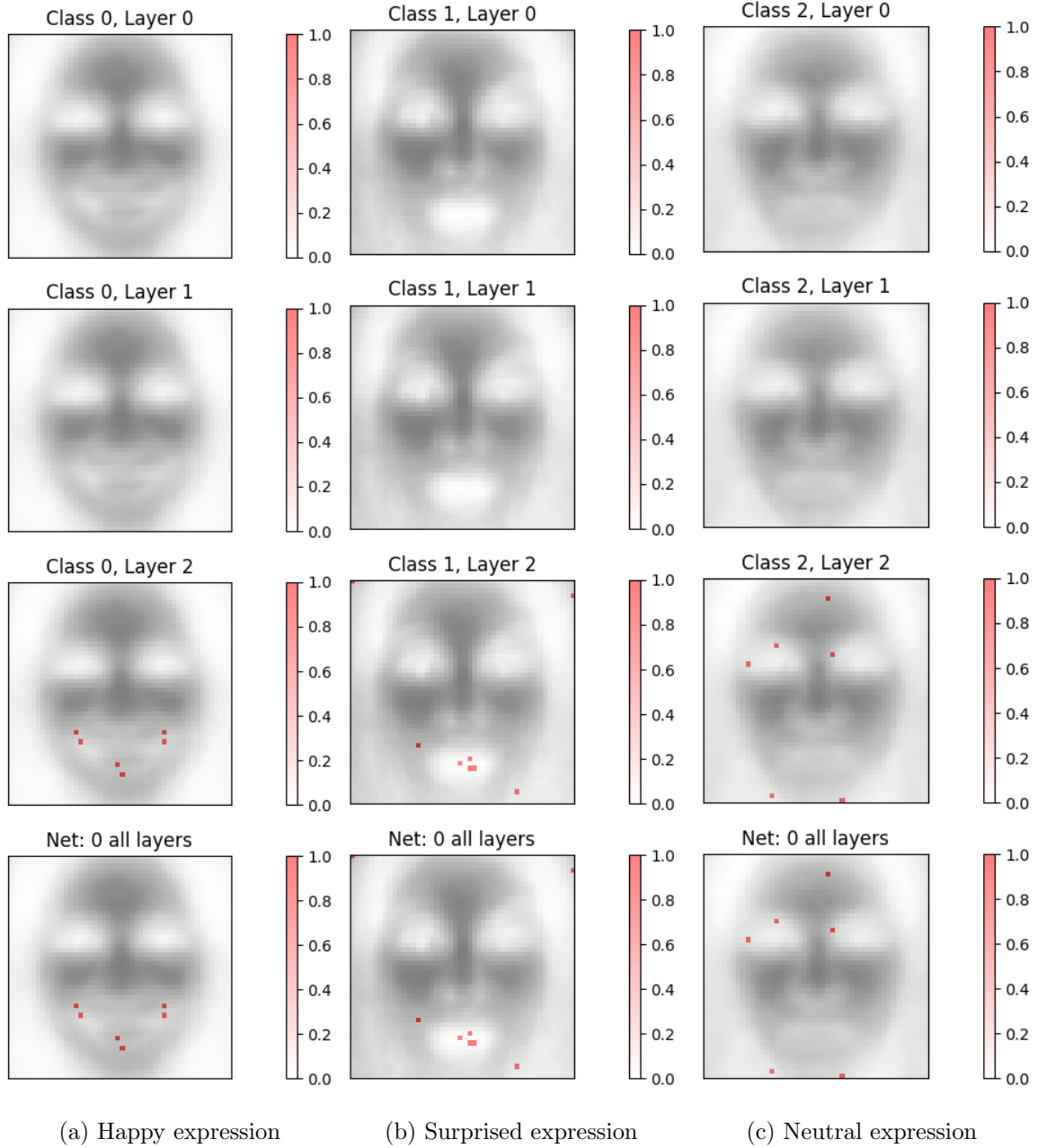


Figure 16: Global explanation of a trained ISLaB-FLOW model showing pixels in the MPM that predict the addressed classes in the FER2013 dataset.

### 3.2.7 MNIST DATASET

The final example in this section is the MNIST dataset from [LeCun et al. \[1998\]](#). The MNIST dataset consists of  $28 \times 28$  images of digits between 0 and 9. The MNIST dataset has established train and test sets, which consist of 60'000 and 10'000 images, respectively. For these experiments, we initiated networks with two hidden layers, each consisting of 600

hidden nodes, giving 1’314’640 weights in the full model. For the L1 regularized networks, we trained networks using four different levels of regularization:  $\lambda = \{0.01, 0.1, 0.2, 1.0\}$ . This is done to illustrate how different regularization levels will induce different sparsity levels and thus different performance results.

From Table 15, we have that the lowest regularization level,  $\lambda = 0.01$ , gives higher accuracies than the networks with the highest regularization,  $\lambda = 1.0$ . However, this comes at the cost of including approximately 11 times the amount of weights and using a much more complex network structure, as indicated by the average and max depth metrics. We see that with the stronger regularizations, the ANN becomes a linear model, with accuracies comparable to our linear Bayesian baselines (but still using more weights). We note that the ISLaB-FLOW method is able to get almost 97 % accuracy, while only using around 900 weights (of a possible 1’314’640) corresponding to over 99.9% sparsification. This is impressive, as it hardly uses more weights than the linear methods, but still includes many non-linear terms. To our best awareness this is the most sparse neural network model achieving over 96% accuracy on MNIST data.

The calibration results displayed in Table 16 show that the ISLaB-FLOW method has the best ECE (while also using the fewest number of weights), whereas the frequentist network with the smallest regularization term has the lowest NLL.

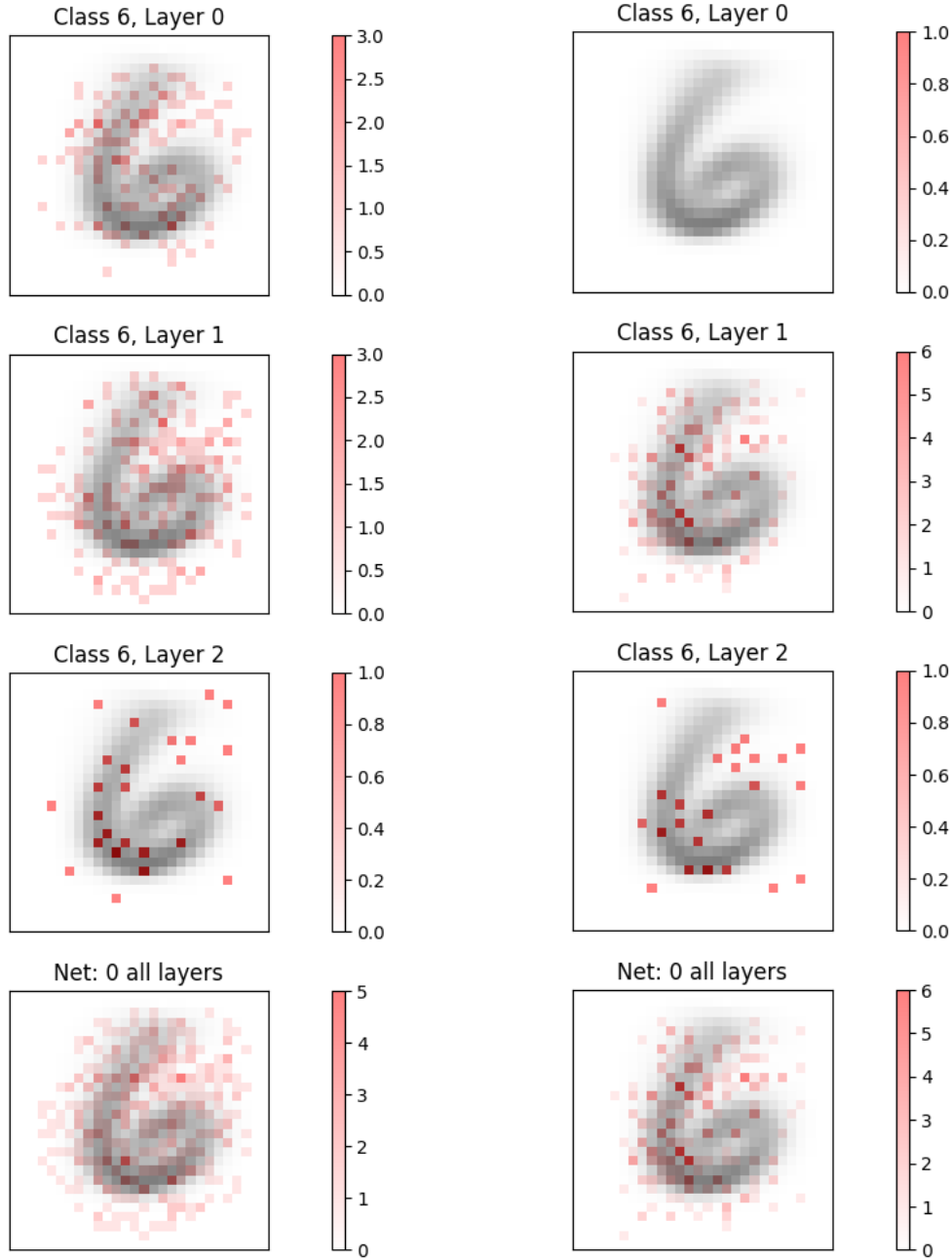
Figure 17 shows the global explanations for predicting digit 6 for an ISLaB-LRT model and an ISLaB-FLOW model. It can be seen that the model focuses on the most relevant regions of the images, as it ignores the redundant information around the edges, and focuses mainly around the center of the image, where the digit typically appears. The two models also seem to focus on crucial regions to distinguish a 6 from any other digit, like the lower left part of the digit, while also focusing on regions where a 6 usually does not attain any pixels, like the upper right part.

Table 15: Results from the MNIST dataset, using two hidden layers consisting of 600 neurons each. The strength of the regularization,  $\lambda$ , is varied to induce different densities for the frequentist network.

Model	ACC, used weights and depth metrics				
	ACC full	ACC sparse	Used weights	Avg depth	Max depth
ISLaB-LRT	96.8 (96.7, 97.0)%	96.5 (96.4, 96.8)%	1157.5 (1112, 1258)	1.94 (1.89, 1.98)	3 (3, 3)
ISLaB-FLOW	96.7 (96.6, 97.1)%	96.7 (96.5, 97.0)%	886.5 (824, 935)	1.65 (1.62, 1.72)	3 (2, 3)
BLR-LRT	92.0 (91.9, 92.2)%	91.9 (91.9, 92.2)%	593.0 (581, 604)	1 (-,-)	1 (-,-)
BLR-FLOW	91.9 (88.2, 92.3)%	91.9 (86.0, 92.1)%	606.0 (585, 666)	1 (-,-)	1 (-,-)
IS-ANN-L1, $\lambda = 1$	90.6 (90.3, 90.7)%	90.6 (90.5, 90.6)%	1092.5 (1076, 1106)	1.00 (1.00, 1.00)	1 (1, 1)
IS-ANN-L1, $\lambda = 0.2$	92.3 (92.1, 92.4)%	92.2 (92.1, 92.2)%	1839.5 (1808, 1853)	1.00 (1.00, 1.00)	1 (1, 1)
IS-ANN-L1, $\lambda = 0.1$	92.7 (92.3, 94.4)%	92.4 (92.2, 93.9) %	2196.0 (2169, 2701)	1.00 (1.00, 1.24)	1 (1, 2)
IS-ANN-L1, $\lambda = 0.01$	98.3 (98.2, 98.4) %	98.4 (98.2, 98.4) %	12276.0 (10968, 13023)	1.91 (1.86, 2.06)	3 (2, 3)

### 3.3 Local explanations

If a network employs activation functions that allow for linear contributions to the output, like the ReLU function, local explanations can be obtained for all predictions, as described in Section 2.7. Additionally, since ISLaB models use variational distributions to describe each weight, credibility intervals can be retrieved for each covariate contribution, alongside a credibility interval for the prediction. Hence, to illustrate this process and demonstrate how it can be plotted, several examples of local explanations will be presented based on



(a) LRT model.

(b) FLOW model.

Figure 17: Pixels used for predicting digit 6 in both ISLaB-LRT and ISLaB-FLOW implementations. Layer 0 indicates all pixels used in the input layer, while Layer 1 and Layer 2 indicate pixels used when the input skips to the respective layers. The last image shows all pixels utilized throughout the model. The 6 digit displayed is an average over all 6 images available in the train set.

Table 16: Expected calibration error and NLL on MNIST.

Model	Ece and NLL			
	ECE full	ECE sparse	NLL	NLL sparse
ISLaB-LRT	0.010 (0.006, 0.012)	0.010 (0.008, 0.011)	0.161 (0.151, 0.168)	0.152 (0.144, 0.161)
ISLaB-FLOW	0.005 (0.002, 0.009)	0.005 (0.003, 0.009)	0.135 (0.118, 0.155)	0.129 (0.114, 0.144)
BLR-LRT	0.019 (0.017, 0.020)	0.018 (0.015, 0.019)	0.311 (0.303, 0.320)	0.305 (0.301, 0.308)
BLR-FLOW	0.021 (0.018, 0.063)	0.019 (0.017, 0.061)	0.327 (0.310, 2.033)	0.316 (0.307, 2.515)
ANN-L1, $\lambda = 1$	0.075 (0.073, 0.077)	0.077 (0.077, 0.078)	0.337 (0.335, 0.341)	0.357 (0.356, 0.357)
ANN-L1, $\lambda = 0.2$	0.035 (0.033, 0.037)	0.036 (0.035, 0.037)	0.276 (0.275, 0.279)	0.286 (0.285, 0.288)
ANN-L1, $\lambda = 0.1$	0.026 (0.021, 0.027)	0.028 (0.019, 0.029)	0.265 (0.191, 0.268)	0.277 (0.214, 0.283)
ANN-L1, $\lambda = 0.01$	0.008 (0.007, 0.010)	0.008 (0.007, 0.009)	0.050 (0.043, 0.061)	0.055 (0.053, 0.057)

three of the problems introduced above. Since the focus in this subsection is purely on displaying examples, we will only focus on an LRT-based ISLaB method in this section. Local experiments can be found and reproduced from [https://github.com/eirihoyh/ISLaB-LBBNN/implementations/local\\_explain](https://github.com/eirihoyh/ISLaB-LBBNN/implementations/local_explain).

### 3.3.1 LINEAR FUNCTION

In the first experiment under consideration, an ISLaB-LRT model with ReLU activations will be trained on the linear problem presented in Section 3.2.1. The model will have 4 hidden layers with 20 hidden nodes per layer. The global explanation of the network after training is displayed in Figure 18, and it attained an accuracy of 99.9%.

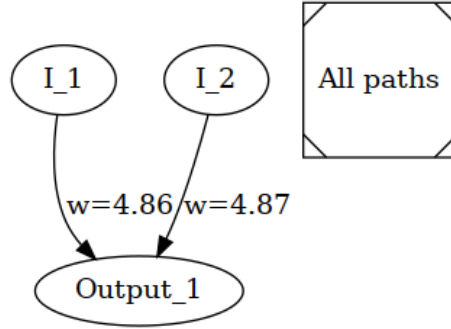


Figure 18: Global explanation of the ISLaB-LRT network trained on the linear problem. The  $w$  indicates the mean of the probability distribution of the weights.

Figure 19 shows the local explanations, in terms of the explainable slope coefficients, of three observations using the empirical sampling based approach delineated in Section 2.7. As can be seen in the figures, it is clear that we retrieved the same slope coefficients for all three explanations, regardless of the final prediction. This indicates that the model has found a linear relationship between the input covariates and the output nodes as the magnitude of the coefficients does not change for different inputs. We can also note that the reason for the uncertain prediction in Figure 19c is due to the input covariates contributing with about the same magnitude to the prediction, but with different signs.

Figure 20 shows the explainable slope coefficients retrieved using the gradients instead of an empirical approach, which is displayed in Figure 19. From this, we can see that the gradient-based method yields the exact same results as the empirical approach, which

underscores that Corollary 2 holds. Note that the gradient based approach is both more scalable and straight forward in terms of implementation and thus should be preferred in practice.

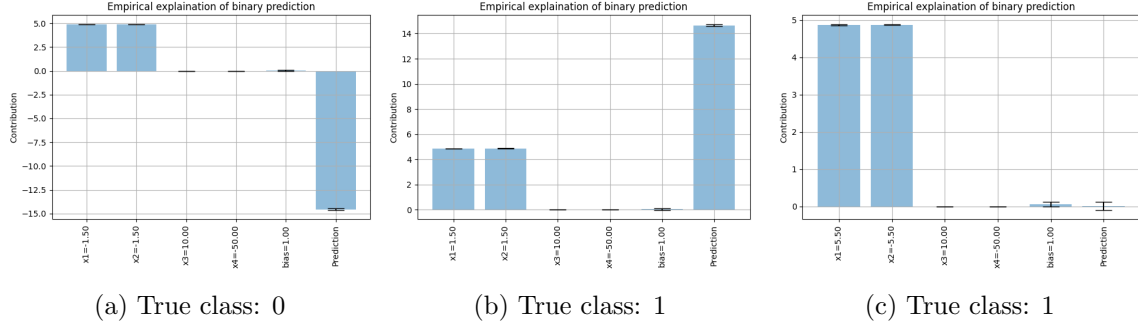


Figure 19: ISLaB-LRT model with empirical explanations of linear problems. The mean impact is displayed as a blue bin in the histogram plot, while the 95% credibility interval is illustrated as error bars on top of each bin. Note that Y-axes are on different scales for (a), (b), and (c).

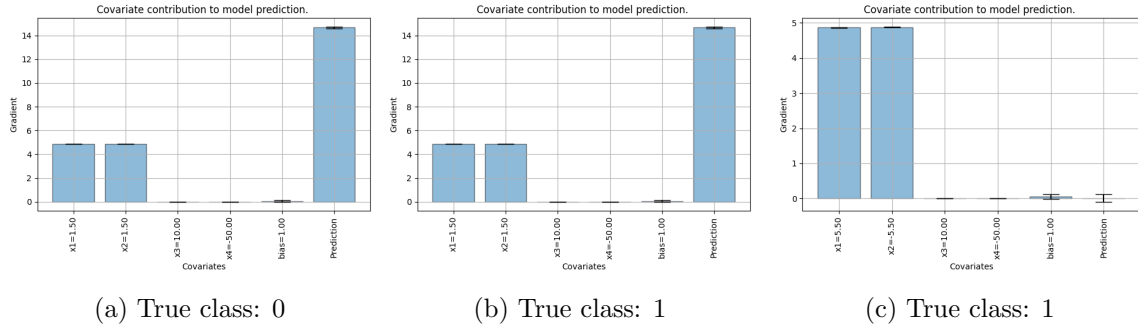


Figure 20: ISLaB-LRT model with gradient explanations of linear problems. The mean impact is displayed as a blue bin in the histogram plot, while the 95% credibility interval is illustrated as error bars on top of each bin.

### 3.3.2 ABALONE DATASET

To obtain local explanations of the predictions of the abalone dataset, a ReLU-activated ISLaB-LRT model will be trained, comprising two hidden layers and 200 hidden nodes per layer. The global explanation of the trained network is found in Figure 21, and it attained an RMSE of 2.07 for the median probability model.



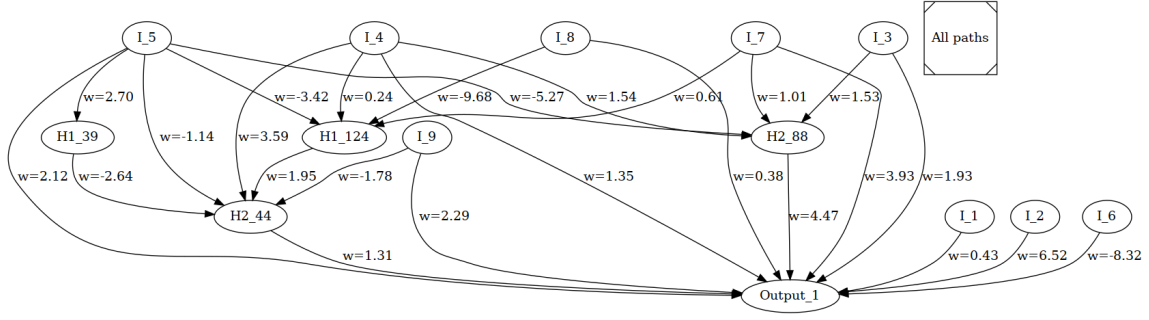


Figure 21: Global explanation of the ISLaB-LRT network trained on the abalone dataset. The  $w$  indicates the mean of the probability distribution of the weights.

The local explanations of observations with 8, 10, and 11 rings are shown in Figure 22. Since this is a regression problem, the covariate contributions can be interpreted more directly, as the magnitude indicates how much each covariate influences the regression model to give its ring count prediction. A notable observation, which does not appear in the previous linear example, is that the selected covariates contributions vary across the problems presented. For instance, the slope coefficients for the *Shucked weight* covariate are different for all three examples, which indicates that different active paths have been activated.

The bias contribution to the prediction, illustrated in Figure 22, is more pronounced than that observed in the previous classification problem, shown in Figure 19. This observation is reasonable as the trained model for the abalone dataset is non-linear, which will make the bias vary more. Also, since the previous problem was a linear classification problem, only the input covariates needed to be considered as the bias will remain constant for all inputs. We will again note that the gradient-based approach, displayed in Figure 23, gives equivalent explanations to the predication as the empirical approach, shown in Figure 22.

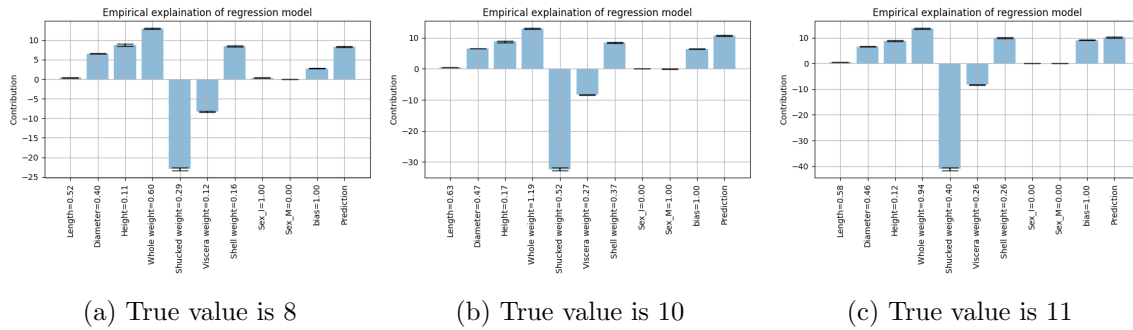


Figure 22: ISLaB-LRT model with empirical explanations of abalone predictions.

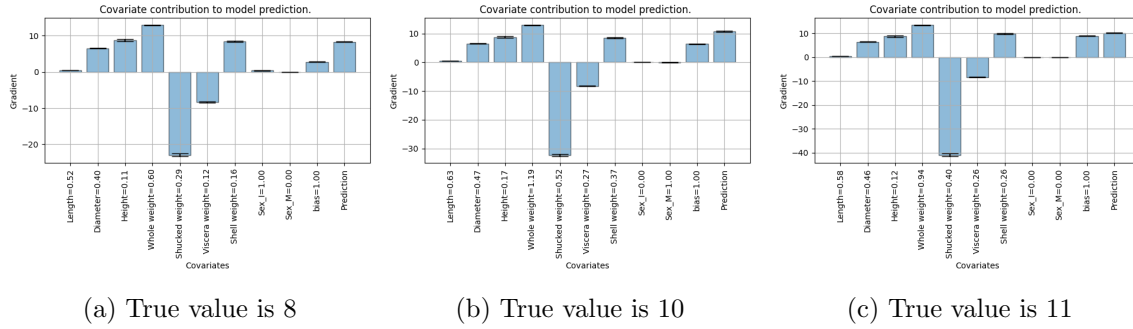


Figure 23: ISLaB-LRT model with gradient explanations of abalone predictions.

### 3.3.3 MNIST DATASET

For the MNIST dataset, a ReLU-based ISLaB-LRT network will be initiated with two hidden layers and 600 hidden nodes per layer. The trained network contains 1'115 weights in the median probability model and obtained an accuracy of 95.47%.

Local explanations of a 4-digit and a 7-digit obtained through the gradient approach are displayed in Figure 24 and 25, where the contributions for class 0, 4, and 7 are explained in sub-figures (a), (b) and (c), respectively. For instance, Figure 24b presents the local explanations for predicting a 4 when a 7 digit is sent through the network. As can be seen in the top part of that image, present pixels give negative contributions, as these are regions where pixels are not typically observed when predicting for the 4 class. On the other hand, for the local explanation of predicting the 7 as a 7 in Figure 24c, this part contributes positively as these are areas where pixels are usually observed for sevens.

For the local explanation of class 0, both Figure 24a and Figure 25a show that having pixels around the middle of the image contributes negatively. This seems reasonable as the observed zeros in the training dataset do not usually have any pixels in this region as they are centered. Hence, when pixels are in the center of the image, the model will push the prediction toward not belonging to the zero class.

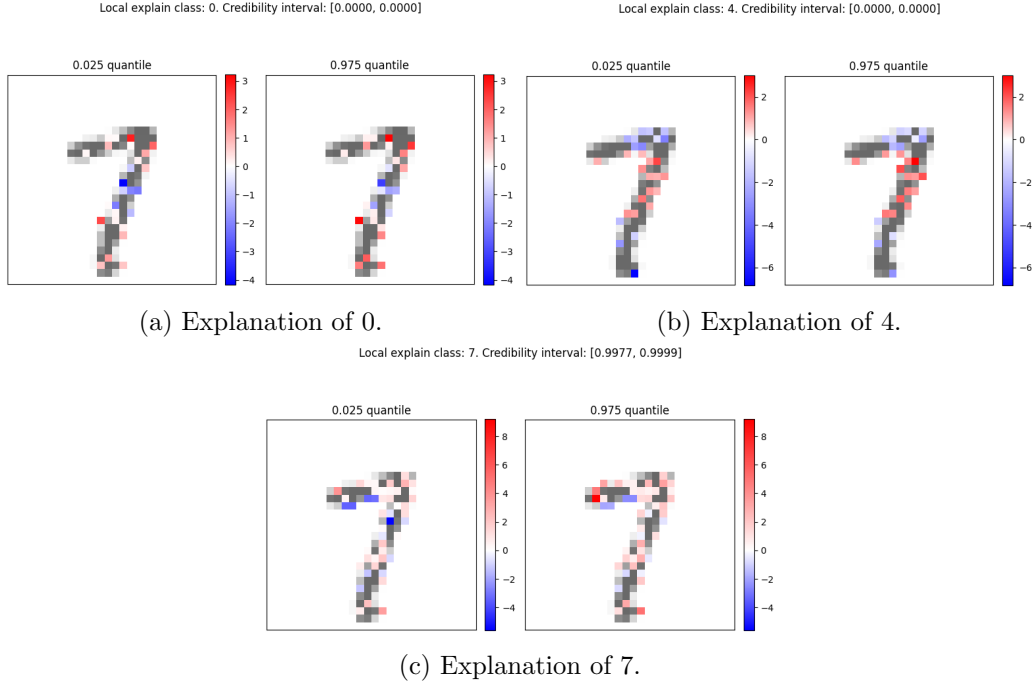


Figure 24: ISLaB-LRT method with gradient explanations of a digit. The true class is seven and the credibility interval is the  $[0.025, 0.975]$  quantiles for the prediction probability.

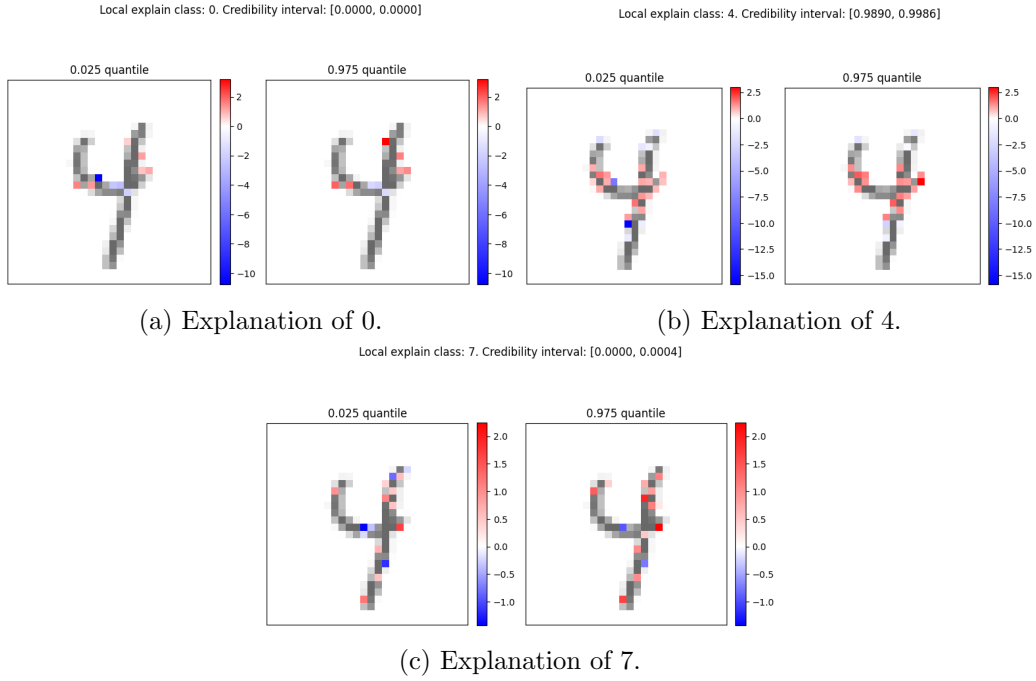


Figure 25: ISLaB-LRT method with gradient explanations of a digit. The true class is four and the credibility interval is the  $[0.025, 0.975]$  quantiles for the prediction probability.

## 4. Discussion

This work has predominantly focused on latent binary Bayesian neural networks (LBBNNs) with input skip, referred to as ISLaB, and has demonstrated how a sparser representation of the network can provide both global and local explanations of predictions. This is mainly accomplished through the concept of active paths, where a trained network is evaluated solely on weights in active paths. The evaluation of networks through active paths and the allowance for entire layers to be deemed redundant has proven to yield simpler structures than previous implementations. For instance, the reported density for the median probability model of an LBBNN-LRT network trained on the MNIST dataset was found to be around 10% in Skaaret-Lund et al. [2024], whereas this work demonstrates that the density can be further reduced to about 0.09% if the ISLaB method is employed and only weights in active paths are considered.

A sparser representation, in conjunction with the model’s ability to deem layers as redundant, can lead to more interpretable models globally as it becomes easier to see which input covariates are used, how many non-linear activations are employed, and how the input covariates interact when contributing to the output. Moreover, as local explanations can be obtained through the use of active paths and piecewise-linear activation functions, information about the covariate contribution can be acquired from each specific prediction. In the context of a Bayesian neural network, it is also possible to derive a full distribution for each covariate local contribution. These explanations differ from those obtained from post-hoc models as both local and global explanations are obtained directly from the predictive model. This is advantageous as it ensures that the obtained explanations are derived from the predictive model. It should be mentioned that local explanations describe how covariates contribute to the predictive node, not how covariates interact and affect each other within the network. It is therefore advantageous to evaluate the local explanations in the context of the global explanation.

In terms of the performance metrics, our proposed ISLaB methods demonstrate excellent performance across multiple datasets, achieving a very good balance between predictive accuracy, model sparsity, interpretability, and uncertainty calibration.

In simulated linear experiments, ISLaB-LRT and ISLaB-FLOW consistently achieve near-perfect accuracy (99.9%) while using only 2-3 active weights and a depth of 1, corresponding to the data-generative model, which is significantly better than IS-ANN-L1, which at the same level of accuracy retains around 8 weights and a depth of 2. The results of linear models here are similar to ISLaBs, which did not make any explicit assumptions on the linearity of the problem. The calibration performance of ISLaBs here was also on par with the linear models, which are optimal for this problem. Variable selection of all methods was similar and almost perfect, with some false positives appearing at high correlation levels.

For non-linear simulated data, ISLaB-LRT and ISLaB-FLOW maintain high accuracy (99.8%) while using 45-85 active weights at an average depth of around 2, whereas IS-ANN-L1 uses 29-35 weights at a similar depth, demonstrating superior sparsification of the latter method. However, calibration scores and variable selection are significantly better for ISLaBs. Linear models for this dataset do not perform well in terms of predictions, as expected, since they cannot handle nonlinearities.

For classification tasks on real datasets, ISLaB-FLOW reaches 97% accuracy on MNIST while using less than a thousand weights, thus much fewer than IS-ANN-L1 or any other known, at the time of writing, neural network with similar performance to our best awareness (thus providing a state of the art in this sense). At the same level of sparsity, IS-ANN-L1 achieves an accuracy of only around 91%, which is worse than what linear models do. A similar pattern is observed for other classification problems, where ISLaB models as a rule demonstrate strong performance across, typically achieving comparable accuracy to IS-ANN-L1 while significantly improving sparsification and often calibration. While IS-ANN-L1 slightly outperforms ISLaB on the Mice Protein dataset, it does so with a much higher parameter count.

For the regression task, ISLaB-LRT achieves the lowest root mean squared error (RMSE) of 2.08 and the lowest pinball loss on the Abalone dataset, while using just around 25 weights on average, confirming its strong predictive capabilities. ISLaB-FLOW has slightly worse performance, yet on par with IS-ANN-L1, but using just 11 weights on average vs 696 for the latter. Linear models perform worse for this problem in terms of both RMSE and calibration, which has been previously noticed in [Hubin et al. \[2021\]](#).

#### 4.1 Initialization and optimization

The initialization of inclusion probabilities in ISLaB plays a crucial role in shaping its learning dynamics and structural sparsification. A dense initialization, where most connections start active (e.g., probabilities close to 1), mimics a backward selection strategy [[Hastie et al., 2009](#), [Sutter and Kalivas, 1993](#), [Burdon and Kumar, 2004](#)], allowing the model to refine its structure by progressively pruning unnecessary paths during training, often resulting in better predictive power but higher density of the model. Conversely, sparse initialization (e.g., probabilities near 0) is more akin to forward selection [[Hastie et al., 2009](#), [Sutter and Kalivas, 1993](#), [Burdon and Kumar, 2004](#)], where only the most critical paths are activated incrementally, often resulting in lighter models but with somewhat lower predictive power. In general, sensitivity to initialization is consistent with previous findings that standard optimization methods such as SGD and Adam may struggle with neural network optimization in the absence of well-informed starting points [[Goodfellow et al., 2016](#), [Sutskever et al., 2013](#)]. Poor initialization can lead to suboptimal minima [[Choromanska et al., 2015](#)], underscoring the importance of strategically setting prior inclusion probabilities. On one hand, this challenge extends beyond LBBNNs and ISLaB to all neural networks—efficient convergence requires initialization schemes that align with both the structure and task [[Glorot and Bengio, 2010](#)], but on the other hand motivates future work on customized optimization designed specifically for LBBNNs and ISLaB. Such future work could explore adaptive initialization strategies, where inclusion probabilities are aggressively adjusted based on early training dynamics, or mode jumping optimization strategies like in mode jumping MCMCs [[Hubin and Storvik, 2018](#), [Tjelmeland and Hegstad, 2001](#)] allowing for multiple restarts guided by reversible Markov Chain to further improve model convergence under any initialization.

## 4.2 Similar work

The work presented in this paper is an extension of the framework already created by Hubin and Storvik [2024] and Skaaret-Lund et al. [2024]. In the LBBNN framework, both weight and structural uncertainty are incorporated into the model, which provides a measure of predictive uncertainty and allows for sparser representations of the network to be formed, respectively. Although this work reports sparser representations and densities compared to those found in earlier studies, it does not necessarily imply a noteworthy difference in the methods. Rather, it underscores the importance of active paths, as this ensures that only weights used for predictions are evaluated. However, an important distinction in this work is the introduction of input-skip, which allows active paths to be formed much closer to the output. This could potentially render earlier layers redundant, thereby giving sparser representations than what had been achievable with an LBBNN that is initialized with the same amount of layers and hidden nodes.

In the finalization of this work, we became aware of other methods that bear resemblance to the active path framework presented in this paper, such as critical data routing paths [Wang et al., 2018], critical pathways [Khakzar et al., 2021], and activation patterns [Raghu et al., 2017]. However, none of these methods define active paths through the inclusion and exclusion of weights within a network, and they do not take into account uncertainty. Also, Sudjianto et al. [2020] proposed a method for obtaining local explanations by unwrapping ReLU-based networks through local linear models and activation patterns. This approach diverges from the work conducted in this paper as active paths are employed to obtain local explanations.

## References

- J. Bai, Q. Song, and G. Cheng. Efficient variational inference for sparse deep learning with theoretical guarantee. In *Advances in Neural Information Processing Systems*, volume 33, pages 466–476, 2020.
- M. M. Barbieri and J. O. Berger. Optimal predictive model selection. *The annals of statistics*, 32(3):870–897, 2004.
- R. Burdon and S. Kumar. Forwards versus backwards selection: trade-offs between expected genetic gain and risk avoidance. *NZ J. For. Sci.*, 34(1):3–21, 2004.
- A. Choromanska, M. Henaff, M. Mathieu, G. B. Arous, and Y. LeCun. The loss surfaces of multilayer networks. In *Artificial intelligence and statistics*, pages 192–204. PMLR, 2015.
- Y. Chung, W. Neiswanger, I. Char, and J. Schneider. Beyond pinball loss: Quantile methods for calibrated uncertainty quantification. *Advances in Neural Information Processing Systems*, 34:10971–10984, 2021.
- I. Covert, S. M. Lundberg, and S.-I. Lee. Understanding global feature contributions with additive importance measures. In *Advances in Neural Information Processing Systems*, volume 33, pages 17212–17223, 2020.
- G. Cybenko. Approximation by superpositions of a sigmoidal function. *Mathematics of Control, Signals and Systems*, 2(4):303–314, 1989.

- T. Elsken, J. H. Metzen, and F. Hutter. Neural architecture search: A survey. *Journal of Machine Learning Research*, 20(55):1–21, 2019.
- D. Erhan, I. Goodfellow, W. Cukierski, and Y. Bengio. Challenges in representation learning: Facial expression recognition challenge, 2013. Online: <https://kaggle.com/competitions/challenges-in-representation-learning-facial-expression-recognition-challenge>; accessed 01.05.2024.
- J. Frankle and M. Carbin. The lottery ticket hypothesis: Finding sparse, trainable neural networks. In *International Conference on Learning Representations*, 2019.
- X. Glorot and Y. Bengio. Understanding the difficulty of training deep feedforward neural networks. In *Proceedings of the thirteenth international conference on artificial intelligence and statistics*, pages 249–256. JMLR Workshop and Conference Proceedings, 2010.
- I. Goodfellow, Y. Bengio, A. Courville, and Y. Bengio. *Deep learning*, volume 1. MIT press Cambridge, 2016.
- C. Guo, G. Pleiss, Y. Sun, and K. Q. Weinberger. On calibration of modern neural networks. In *International conference on machine learning*, pages 1321–1330. PMLR, 2017.
- T. Hastie, R. Tibshirani, and J. Friedman. *The elements of statistical learning*. New York, New York, Springer, 2 edition, 2009. ISBN 9780387848570.
- C. Higuera, K. Gardiner, and K. Cios. Mice Protein Expression. UCI Machine Learning Repository, 2015a. DOI: <https://doi.org/10.24432/C50S3Z>.
- C. Higuera, K. J. Gardiner, and K. J. Cios. Self-organizing feature maps identify proteins critical to learning in a mouse model of down syndrome. *PloS one*, 10(6):e0129126, 2015b.
- K. Hornik, M. Stinchcombe, and H. White. Multilayer feedforward networks are universal approximators. *Neural Networks*, 2(5):359–366, 1989.
- G. Huang, Z. Liu, L. Van Der Maaten, and K. Q. Weinberger. Densely connected convolutional networks. In *Proceedings of the IEEE Conference on Computer Vision and Pattern Recognition*, pages 4700–4708, 2017.
- A. Hubin and G. Storvik. Mode jumping mcmc for bayesian variable selection in glmm. *Computational Statistics & Data Analysis*, 127:281–297, 2018.
- A. Hubin and G. Storvik. Combining model and parameter uncertainty in Bayesian neural networks. *arXiv preprint arXiv:1903.07594*, 2019.
- A. Hubin and G. Storvik. Sparse Bayesian neural networks: Bridging model and parameter uncertainty through scalable variational inference. *Mathematics*, 12(6):788, 2024.
- A. Hubin, G. Storvik, and F. Frommlet. Flexible Bayesian nonlinear model configuration. *Journal of Artificial Intelligence Research*, 72:901–942, 2021.

- A. Hubin, G. Heinze, and R. De Bin. Fractional polynomial models as special cases of Bayesian generalized nonlinear models. *Fractal and Fractional*, 7(9):641, 2023.
- C. Jiang, C. Jiang, D. Chen, and F. Hu. Densely connected neural networks for nonlinear regression. *Entropy*, 24(7):876, 2022.
- A. Khakzar, S. Baselizadeh, S. Khanduja, C. Rupprecht, S. T. Kim, and N. Navab. Neural response interpretation through the lens of critical pathways. In *Proceedings of the IEEE/CVF Conference on Computer Vision and Pattern Recognition*, pages 13528–13538, 2021.
- D. P. Kingma and J. Ba. Adam: A method for stochastic optimization. In *International Conference on Learning Representations*, 2015.
- D. P. Kingma, T. Salimans, and M. Welling. Variational dropout and the local reparameterization trick. In *Advances in Neural Information Processing Systems*, volume 28, 2015.
- Y. LeCun, L. Bottou, Y. Bengio, and P. Haffner. Gradient-based learning applied to document recognition. *Proceedings of the IEEE*, 86(11):2278–2324, 1998.
- C. Louizos and M. Welling. Multiplicative normalizing flows for variational Bayesian neural networks. In *Proceedings of the 34th International Conference on Machine Learning*, pages 2218–2227. PMLR, 2017.
- S. M. Lundberg and S.-I. Lee. A unified approach to interpreting model predictions. In *Advances in Neural Information Processing Systems*, volume 30, pages 4765–4774, 2017.
- E. T. B. Lundby, H. Robinson, A. Rasheed, I. J. Halvorsen, and J. T. Gravdahl. Sparse neural networks with skip-connections for identification of aluminum electrolysis cell. In *IEEE Conference on Decision and Control*, pages 5506–5513, 2023.
- W. Nash, T. Sellers, S. Talbot, A. Cawthorn, and W. Ford. Abalone. UCI Machine Learning Repository, 1995. DOI: <https://doi.org/10.24432/C55C7W>.
- R. M. Neal. Bayesian training of backpropagation networks by the hybrid Monte Carlo method. Technical report, Citeseer, 1992.
- OpenAI. Gpt-4 technical report. *arXiv preprint arXiv:2303.08774*, 2023.
- T. Papamarkou, M. Skoularidou, K. Palla, L. Aitchison, J. Arbel, D. Dunson, M. Filippone, V. Fortuin, P. Hennig, J. M. Hernández-Lobato, et al. Position: Bayesian deep learning is needed in the age of large-scale ai. In *Forty-first International Conference on Machine Learning*, 2024.
- M. Raghu, B. Poole, J. Kleinberg, S. Ganguli, and J. Sohl-Dickstein. On the expressive power of deep neural networks. In *Proceedings of the 34th International Conference on Machine Learning*, volume 70, pages 2847–2854. PMLR, 2017.



- O. Ronneberger, P. Fischer, and T. Brox. U-net: Convolutional networks for biomedical image segmentation. In *Medical Image Computing and Computer-Assisted Intervention*, pages 234–241. Springer, 2015.
- A. Shrikumar, P. Greenside, A. Shcherbina, and A. Kundaje. Not just a black box: Learning important features through propagating activation differences. *arXiv preprint arXiv:1605.01713*, 2016.
- A. Shrikumar, P. Greenside, and A. Kundaje. Learning important features through propagating activation differences. In *Proceedings of the 34th International Conference on Machine Learning*, volume 70, pages 3145–3153. PMLR, 2017. URL <https://proceedings.mlr.press/v70/shrikumar17a.html>.
- L. Skaaret-Lund, G. Storvik, and A. Hubin. Sparsifying Bayesian Neural Networks with Latent Binary Variables and Normalizing Flows. *Transactions on Machine Learning Research*, 10 2024. URL <https://openreview.net/forum?id=d6kqUKzG3V>.
- A. Sudjianto, W. Knauth, R. Singh, Z. Yang, and A. Zhang. Unwrapping the black box of deep ReLU networks: Interpretability, diagnostics, and simplification. *arXiv preprint arXiv:2011.04041*, 2020.
- I. Sutskever, J. Martens, G. Dahl, and G. Hinton. On the importance of initialization and momentum in deep learning. In *International conference on machine learning*, pages 1139–1147. PMLR, 2013.
- J. M. Sutter and J. H. Kalivas. Comparison of forward selection, backward elimination, and generalized simulated annealing for variable selection. *Microchemical journal*, 47 (1-2):60–66, 1993.
- H. Tjelmeland and B. K. Hegstad. Mode jumping proposals in mcmc. *Scandinavian journal of statistics*, 28(1):205–223, 2001.
- Y. Wang, H. Su, B. Zhang, and X. Hu. Interpret neural networks by identifying critical data routing paths. In *Proceedings of the IEEE Conference on Computer Vision and Pattern Recognition*, pages 8906–8914, 2018.
- W. Wolberg, O. Mangasarian, N. Street, and W. Street. Breast cancer Wisconsin (diagnostic). UCI Machine Learning Repository, 1995. DOI: <https://doi.org/10.24432/C5DW2B>.

## Appendix A. Hyperparameters and initialization

Table 17: Initial inclusion probability,  $\alpha = 1/(1+\exp(-\lambda))$ , for all weights. Initial values are drawn from uniform distributions,  $\lambda \sim \text{Unif}(\lambda_{\min}, \lambda_{\max})$ , and we separate the initialization into weights, which are connections going from hidden nodes, and covariate, which are connections coming from a covariate. We draw  $\lambda$  from the same probability distribution regardless of the position in the network. That is, the same distribution is used for connections in, e.g., the first hidden layer and the last hidden layer.

Experiment	$\lambda_{\min}$ weights	$\lambda_{\max}$ weights	$\lambda_{\min}$ covariates	$\lambda_{\max}$ covariates
Sim. lin. - LRT	-10	-7	5	5
Sim. lin. - FLOW	-10	-7	5	5
Sim. lin. - BLR-LRT	-	-	0	1
Sim. lin. - BLR-FLOW	-	-	0	1
Sim. nonlin. - LRT	-5	-4	5	5
Sim. nonlin. - FLOW	4	6	5	15
Sim. nonlin. - BLR-LRT	-	-	0	1
Sim. nonlin. - BLR-FLOW	-	-	0	1
WBC - LRT	-9	-5	5	5
WBC - FLOW	-9	-5	5	15
WBC - BLR-LRT	-	-	0	1
WBC - BLR-FLOW	-	-	0	1
Abalone - LRT	-9	-4	5	5
Abalone - FLOW	-9	-4	5	5
Abalone - BLR-LRT	-	-	0	1
Abalone - BLR-FLOW	-	-	0	1
MiM prot. - LRT	10	15	10	15
MiM prot. - FLOW	10	15	10	15
MiM prot. - BLR-LRT	-	-	10	15
MiM prot. - BLR-FLOW	-	-	10	15
MNIST - LRT	5	15	5	15
MNIST - FLOW	10	15	10	15
MNIST - BLR-LRT	-	-	0	1
MNIST - BLR-FLOW	-	-	0	1
FER2013 - LRT	-8	-6	-8	-6
FER2013 - FLOW	-8	-6	-8	-6
FER2013 - BLR-LRT	-	-	0	1
FER2013 - BLR-FLOW	-	-	0	1

Table 18: Hyperparameters and tuning parameters used in the experiments.  $p(w)$  denotes the prior weight distribution,  $\psi$  represents the prior inclusion probability for all weights, "lr." is the learning rate, "Max epochs" refers to the maximum training epochs, "Patience" indicates epochs without improvement in validation accuracy before termination, and "Burn-in" is the number of epochs for model initialization. "Iter. per epoch" is the number of iterations per epoch, corresponding to the number of batches the training dataset is divided into, and "Lik" is the likelihood function used for modeling the responses, with N for normal, B for Bernoulli, and C for Categorical. For the flow-based methods, we use two transformations.

Experiment	$p(w)$	$\psi$	lr.	Epochs	Iter. epoch	Lik.
Sim. lin. - LRT	$\mathcal{N}(0, 2.5^2)$	0.001	0.1	200	50	B
Sim. lin. - FLOW	$\mathcal{N}(0, 2.5^2)$	0.001	0.01	200	10	B
Sim. lin. - BLR-LRT	$\mathcal{N}(0, 2.5^2)$	0.001	0.01	200	50	B
Sim. lin. - BLR-FLOW	$\mathcal{N}(0, 2.5^2)$	0.001	0.01	200	50	B
Sim. lin. - ANN-L1	-	-	0.01	750	50	B
Sim. nonlin. - LRT	$\mathcal{N}(0, 30^2)$	0.01	0.01	750	50	B
Sim. nonlin. - FLOW	$\mathcal{N}(0, 30^2)$	0.05	0.01	750	10	B
Sim. nonlin. - BLR-LRT	$\mathcal{N}(0, 30^2)$	0.001	0.01	200	50	B
Sim. nonlin. - BLR-FLOW	$\mathcal{N}(0, 30^2)$	0.001	0.01	200	50	B
Sim. nonlin. - ANN-L1	-	-	0.01	750	50	B
WBC - LRT	$\mathcal{N}(0, 1^2)$	0.01	0.1	200	8	B
WBC - FLOW	$\mathcal{N}(0, 1^2)$	0.01	0.05	200	8	B
WBC - BLR-LRT	$\mathcal{N}(0, 1^2)$	0.01	0.01	200	8	B
WBC - BLR-FLOW	$\mathcal{N}(0, 1^2)$	0.01	0.01	200	8	B
WBC - ANN-L1	-	-	0.01	200	8	B
Abalone - LRT	$\mathcal{N}(0, 25^2)$	0.25	0.01	5,000	5	N
Abalone - FLOW	$\mathcal{N}(0, 25^2)$	0.25	0.01	2,000	5	N
Abalone - BLR-LRT	$\mathcal{N}(0, 25^2)$	0.25	0.005	2,000	5	N
Abalone - BLR-FLOW	$\mathcal{N}(0, 15^2)$	0.25	0.01	2,000	5	N
Abalone - ANN-L1	-	-	0.01	2,000	5	N
MiM prot. - LRT	$\mathcal{N}(0, 25^2)$	0.05	0.01	2,000	27	C
MiM prot. - FLOW	$\mathcal{N}(0, 25^2)$	0.05	0.01	500	27	C
MiM prot. - BLR-LRT	$\mathcal{N}(0, 25^2)$	0.05	0.01	500	27	C
MiM prot. - BLR-FLOW	$\mathcal{N}(0, 25^2)$	0.05	0.01	500	27	C
MiM prot. - ANN-L1	-	-	0.001	20,000	1	C
MNIST - LRT	$\mathcal{N}(0, 15^2)$	0.01	0.01	1,000	50	C
MNIST - FLOW	$\mathcal{N}(0, 10^2)$	0.01	0.005	2,000	50	C
MNIST - BLR-LRT	$\mathcal{N}(0, 15^2)$	0.1	0.01	250	50	C
MNIST - BLR-FLOW	$\mathcal{N}(0, 10^2)$	0.1	0.005	250	50	C
MNIST - ANN-L1	-	-	0.01	250	50	C
FER2013 - LRT	$\mathcal{N}(0, 30^2)$	0.05	0.005	10,000	10	C
FER2013 - FLOW	$\mathcal{N}(0, 30^2)$	0.1	0.0025	10,000	10	C
FER2013 - BLR-LRT	$\mathcal{N}(0, 30^2)$	0.05	0.005	1,000	10	C
FER2013 - BLR-FLOW	$\mathcal{N}(0, 30^2)$	0.1	0.0025	1,000	10	C
FER2013 - ANN-L1	-	-	0.005	1,000	10	C

## Appendix B. Further detail for the mice data

Table 19: The classes, explanation, and content of each class in the mice protein dataset. Explanations are retrieved from [Higuera et al. \[2015a\]](#).

Class description mice protein dataset	
Class name (class nr.)	Description
c-CS-s (1)	control mice, stimulated to learn, injected with saline
c-CS-m (2)	control mice, stimulated to learn, injected with memantine
c-SC-s (3)	control mice, not stimulated to learn, injected with saline
c-SC-m (4)	control mice, not stimulated to learn, injected with memantine
t-CS-s (5)	trisomy mice, stimulated to learn, injected with saline
t-CS-m (6)	trisomy mice, stimulated to learn, injected with memantine
t-SC-s (7)	trisomy mice, not stimulated to learn, injected with saline
t-SC-m (8)	trisomy mice, not stimulated to learn, injected with memantine